applied sciences

MDPI

Review

Photoconductive Semiconductor Switches: Materials, Physics, and Applications

Vincent Meyers [1,*], Lars Voss [2], Jack D. Flicker [1], Luciano Garcia Rodriguez [1], Harold P. Hjalmarson [1], Jane Lehr [3], Nicolas Gonzalez [3], Gregory Pickrell [1], Soroush Ghandiparsi [2] and Robert Kaplar [1]

[1] Sandia National Laboratories, Albuquerque, NM 87123, USA; jdflick@sandia.gov (J.D.F.); lagarc@sandia.gov (L.G.R.); hphjalm@sandia.gov (H.P.H.); gpickre@sandia.gov (G.P.); rjkapla@sandia.gov (R.K.)
[2] Lawrence Livermore National Laboratories, Livermore, CA 94550, USA; voss5@llnl.gov (L.V.); ghandiparsi1@llnl.gov (S.G.)
[3] Department of Electrical and Computer Engineering, University of New Mexico, Albuquerque, NM 87106, USA; jmlehr@unm.edu (J.L.); negonzalezp2304@unm.edu (N.G.)
* Correspondence: vemeyer@sandia.gov

Abstract: Photoconductive semiconductor switching (PCSS) devices have unique characteristics to address the growing need for electrically isolated, optically gated, picosecond-scale jitter devices capable of operating at high voltage, current, and frequency. The state of the art in material selection, doping, triggering, and system integration in PCSSs is presented. The material properties and doping considerations of GaN, GaAs, SiC, diamond, and β-Ga_2O_3 in the fabrication of PCSS devices are discussed. A review of the current understanding of the physics of the high-gain mode known as lock-on is presented.

Keywords: GaN; photoconductive switch; high-voltage switching

Academic Editor: Gerard Ghibaudo

Received: 23 November 2024
Revised: 21 December 2024
Accepted: 23 December 2024
Published: 10 January 2025

Citation: Meyers, V.; Voss, L.; Flicker, J.D.; Rodriguez, L.G.; Hjalmarson, H.P.; Lehr, J.; Gonzalez, N.; Pickrell, G.; Ghandiparsi, S.; Kaplar, R. Photoconductive Semiconductor Switches: Materials, Physics, and Applications. *Appl. Sci.* **2025**, *15*, 645. https://doi.org/10.3390/app15020645

1. Introduction

Photoconductive semiconductor switches (PCSSs) are optically-gated switches that rely on photogenerated carriers to conduct current through a semiconducting medium between two contacts. While any semiconductor can operate as a PCSS, research has disproportionately focused on GaAs, SiC, and GaN due to their electrical properties (enumerated in Table 1) and technological maturity. PCSSs offer several advantages over conventional high-power switches like spark gaps or insulated-gate bipolar transistors (IGBTs): they can be >10× more compact than a comparable conventional switch, they can be triggered remotely (making them potentially immune to electromagnetic interference), exhibit ps-scale jitter, and avoid the high-pressure gas requirements of spark gaps. Fabrication typically involves a few steps on a substrate doped to be semi-insulating: a single metalization step to form an *m-i-m* structure, and optionally, a dielectric deposition step to suppress surface flashover. Devices can be fabricated in vertical or lateral geometries, with the latter being typically either linear or radial. An overview of switch design and fabrication considerations is available elsewhere and is not the primary focus of this work [1].

The commercial application of devices has been limited due to very short shot lifetimes, being typically not greater than 10^7 for Si, 10^4 for GaAs, and substantially less than this for other materials [2,3]. Future commercialization requires fundamental efforts to understand the impacts of doping and electrode geometry on efficiency and electrical damage.

PCSSs operate in one of two modes. The most common and conceptually straightforward is the linear mode, wherein switch conductivity persists only as long as the optical

gate signal is applied; more exotic and potentially more technologically useful is the nonlinear high-gain mode, to-date observed only in direct bandgap materials [4,5]. PCSS devices fabricated from Si, SiC, Ga_2O_3, and diamond are ubiquitously operated only in linear mode. PCSS devices fabricated with direct-bandgap materials including GaAs, InP, and GaN, in addition to linear mode operation, exhibit a high-gain mode, known as lock-on, wherein a switch closed above a threshold field remains closed after the end of an optical gate signal so long as a critical field (corresponding to the "lock-on field") persists across the switch leads [5,6]. Under appropriate doping and triggering conditions, whether the voltage applied to switches fabricated from the latter group of materials results in a field above (below) a material-specific threshold value determines whether the switch operates in lock-on (linear) mode.

Table 1. Comparison of electrical and thermal properties of semiconducting materials most commonly used in PCSS applications, with a comparison to Si as a baseline material.

Property	Si	GaAs	4H-SiC	GaN	AlN	β-GA_2O_3	Diamond
Bandgap (eV), Direct or Indirect (d, i)	1.11, i	1.43, d	3.26, i	3.39, d	6.1, d	4.5, i	5.47, d or i
Breakdown Electric Field (MV/cm)	0.3	0.4	2.0	3.3	11.7	7	10
Electron Mobility ($cm^2\ V^{-1}s^{-1}$)	1400	8500	700	900	1100	200	4500
Saturation Drift Velocity ($\times 10^7$ cm/s)	1.0	1.0	2.0	2.5	1.8	1.7	2.0
Relative Permittivity	11.8	12.9	9.7	9.5	8.7	10	5.7
Thermal Conductivity (W/cm K)	1.5	0.5	4.5	1.3	2.5	0.2	2.2
Maximum Operable Junction Temperature (°C)	300	300	1600	500	1000	1700	700

Though high gain operation is commonly referred to as lock-on in different material systems, the underlying mechanisms differ by material, as will be discussed in the next section. In this work, we use the term lock-on with the significant caveat that it may require differentiation in the future as an understanding of the fundamental physics of the mode in each material improves. At the circuit-level, high gain operation is material-agnostic; however, the optically-closed switch conductivity remains constant, permitting constant-impedance discharging of the primary until the field dips below the critical value and the switch opens. The origins of this phenomenon have variously been attributed to negative differential conductivity (NDC), avalanche multiplication, and dismissed altogether as surface flashover. It is likely that the bandstructure of each material, provided its bandgap is direct, furnish a material-dependent set of physical mechanisms whereby lock-on occurs; trap-to-band ionization, negative differential mobility (NDM), avalanche injection, and as-yet unidentified surface effects appear most plausible [6–8]. This review paper offers an overview of the current state-of-the-art in materials and applications of PCSS devices, an interrogation of the physics of lock-on, and a detailed example of an implementation of a GaN PCSS operated in high-gain mode in a medium-voltage circuit breaker.

2. Theory of PCSS Operation

The most common mechanism of photoconductive switch operation is the linear mode. In this mechanism, the optically injected electrons and holes produce a photocurrent driven by the electric field. This photocurrent J is proportional to the electric field E, the injected electron (hole) densities, n (p) densities, and their respective mobilities $\mu_{n\ (p)}$ as $J = e(n\mu_n + p\mu_p)E$, where e is the fundamental charge. In this conventional case, the electron and hole densities reach a steady-state density that requires continuous optical

generation and is typically controlled by the density and levels of electronic traps in the material.

In some cases, the optical injection stimulates the generation of electrons and holes in a non-linear way by means of one or a combination of physical mechanisms. For example, above a material-dependent threshold field, an avalanche process generates electrons and holes ("avalanche gain"). Once this process initiates, a sustained optical source is not necessary. Semiconductors in which these non-linear conduction mechanisms can be optically triggered can be used either as linear-mode or high-gain PCSS devices, depending on the field applied. Such switches can be very efficient in principle because the optical trigger is only necessary during the initiation process.

Such switches have been made using the direct bandgap semiconductors GaAs and GaN. The proposed mechanisms are very different. The GaAs mechanism involves a non-linear avalanche mechanism that is determined by unique features of the GaAs band-structure. The GaN switches do not have a bandstructure consistent with this mechanism. Instead, the proposed mechanism involves avalanche injection.

a. Theoretical Foundation for Nonlinear Mode in Direct Bandgap PCSS Devices

To distinguish the origins of lock-on behavior in different materials, a computational comparison of GaN and GaAs is presented. Both sets of calculations are implemented in a structure consisting of a 1D high-resistivity (semi-insulating) region terminated on both ends with identical Ohmic contacts. The semiconductor region is insulating due to a large density of traps caused by impurities. This high resistivity provides the non-conductive off-state that persists in the absence of optical illumination. The steady-state carrier densities during illumination are assumed to be governed by trap capture. The primary common feature to both materials is the physics of the off-state. This state is caused by the defects that trap electrons. These trapped electrons cause an electric field that inhibits the flow of current.

b Computational Approach

Two methods are used: a conventional ensemble Monte Carlo (EMC), and a proprietary solver for coupled transient reactive transport equations called Radiation Effects in Oxides and Semiconductors (REOS) [9]. In both methods, the calculations include the effects of large electrical fields and large carrier densities. Both of these methods enable the interrogation of ab initio physical principles to derive a statistical model of device operation [10]. By simulating particle-level interactions, carrier transport dynamics outside of standard excitation conditions can be self-consistently modelled. These methods each have this advantage over more conventional technology computer aided design (TCAD) software packages.

REOS is used to analyze photocurrent and breakdown by solving the continuum equations. This code computes the temporal electrical response to stimuli applied to a material such as a semiconductor, insulator, or a metal [11,12]. The main external stimulus considered is an electrical current governed by an external circuit. During the simulation session, the sample can be subjected to ionizing radiation, thermal energy, and ion beams. These calculations include defect chemistry, interface effects, tunneling reactions, hot carriers, and lattice heating. These effects are governed by reactive transport equations that have specific terms corresponding to the species flow and the species reactions. The response involves flow and chemical reactions of electrons, holes, and chemical species such as impurities and lattice defects. The species flow is governed by drift-diffusion equations. The reactions are governed by the chemical potentials of the constituents. Additional terms include the effects of the external stimuli. The energy changes are captured in a lattice temperature as well as electron and hole temperatures. The calculations are governed by input information that defines the physical quantities, the initial conditions, the injected

quantities, the reactions, and the electrical circuit. The main computed quantities are the species densities as a function of time and position and the electrical currents as a function of time.

The EMC is a particle-based method that can solve the Boltzmann transport equations governing electrons and holes in a semiconductor [13]. This software differs from conventional particle-based calculations because it includes high-density effects. The code self-consistently implements Fermi exclusion and carrier–carrier scattering. The solution of the Boltzmann equation using a particle method seeks the electron distribution function $f(r, k, t)$ as a function of position r, wavevector k, and time t. The method obtains the solution by following the evolution of the distribution function as electrons respond to an electric field. In addition, these particles scatter by interactions with phonons and other electrons. The accurate simulation of electron–electron scattering is critical for computing breakdown dynamics. At the high carrier densities involved in breakdown, Fermi exclusion must be implemented. Impact ionization rates are computed using both electron–electron scattering and two-electron impact ionization.

c The GaAs mechanism

The initiating optical pulse in the presence of an electric field causes an initial high photoconductivity. These initial carriers, under appropriate conditions, lead to an increased density of charge carriers in continuous regions spanning the contacts [13], termed "filaments". The growth mechanism exhibits avalanche-like behavior. The conductive on-state is maintained by a so-called minimum lock-on electric field E_{LO} = 5 kV/cm. This is quite small compared with the values 100−250 kV/cm reported for the threshold field that must be exceeded to initiate avalanche breakdown in GaAs. The threshold field E_T = 10–30 kV/cm required to initiate lock-on is also small compared with the fields needed to initiate avalanche breakdown in the absence of an optical trigger.

Early studies attributed the self-sustaining current to collective impact ionization [14,15], which involves conventional impact ionization and models the carrier energy distribution function by considering carrier–carrier interactions. This theory leads to qualitative agreement with the lock-on phenomenon. For a given electric field, this mechanism leads to two stable states: a non-conductive off-state and a conductive on-state. These two states correspond to the conductive region of an optically initiated current filament and the non-conductive external region. It fails to predict the magnitude of E_{LO}, however, suggesting a value of E_{LO} = 50 kV/cm that is much lower than the bulk avalanche field. However, this predicted field is 10 times larger than the observed lock-on field [16]. A similar situation has been found for other materials.

This shortcoming of collective impact ionization theory led to a refined version of this theory called two-electron impact ionization [17]. In the mechanism, two electrons in the conduction band share their energy during a collision. A process of this type is responsible for the broadening of the distribution function if the carrier density is sufficiently high. However, in the two-electron mechanism, the more energetic electron undergoes a virtual transition to an excited virtual state. Its final state is a low energy state in the conduction band just as in conventional impact ionization. Instead of impact ionization caused by a single electron, in this theory, the energy of two electrons is combined in an impact ionization event. More precisely, two electrons at nearly the same elevated energies interact with each other. This scattering event causes one to go down in energy and the other one to go up in energy. The state reached by the more energetic electron is a virtual state. The electrons in these virtual states initiate the impact ionization that produces new electron–hole pairs. The end result is impact ionization by two electrons whose shared energy is sufficient to create the electron–hole pair.

The REOS and EMC calculations also include carrier–carrier scattering, which arises from the competing effects of two-electron impact ionization and Auger recombination. These results are consistent with the prediction of the collective impact ionization theory that $E_{LO} < E_T$ and predict the formation of the ubiquitously observed current filaments. Despite over 35 years of repeatable observations of lock-on in GaAs, the combination of mechanisms involved is not fully understood. Additional testing and new calculations will be necessary to assess whether the computed sustaining field approaches the lock-on field.

d The GaN mechanism

The primary mechanism suggested for lock-on in a GaN optically triggered switch involves defects that enhance the field at anode contact. This model relies on acceptor defects that cause both the off-state and the on-state [18]. In the on-state, these defects undergo impact ionization to enable the avalanche injection. They also cause a large field enhancement that causes conventional band-to-band impact ionization.

Early theoretical work that explored the effects of defects showed that impact ionization of the acceptors produced a mechanism for optical initiation of lock-on. However, the simulated current flow during self-sustaining conduction was not appreciably larger than the photocurrent that was used to trigger the lock-on state, indicating that this mechanism in isolation is insufficient. Those earlier calculations led to a revised mechanism. In this mechanism, the primary effect of deep defects is to cause a field enhancement of sufficient magnitude to enable conventional band-to-band impact ionization [7,8,19].

The mechanism has been validated by using it for avalanche breakdown calculations of a reverse biased GaN diode. This model is then used in calculations applied to an *n-i-n* GaN structure. These calculations predict a dramatic switching event from a non-conductive off-state to a highly conductive on-state involving lock-on. The calculations discussed here involve a generalized *n-i-n* structure illustrated in Figure 1. For these calculations, a positive electrical potential is applied to the right-hand contact. This figure shows an *n-i-n* structure that has donor-doped contacts and also heavily doped acceptor regions denoted by p^+. The donor densities in the *n*-regions are 10^{19} cm^{-3}, and the Mn-doped acceptor-like doping is 5×10^{19} cm^{-3}. The total thickness is 2 μm.

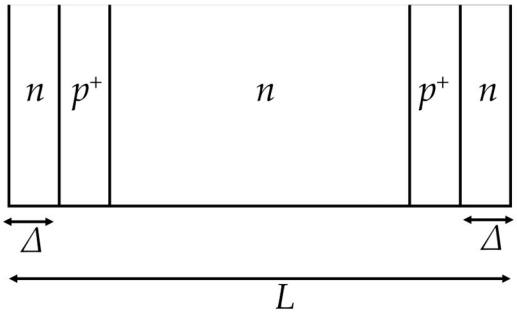

Figure 1. Schematic of doping in a simulated *n-i-n* switch structure.

A series of calculations explored the effects of Mn acceptor-like defects [20]. The first role of the acceptors is to trap the injected electrons. The resultant electric field halts the injection of additional electrons. The trapped charge produces a space charge barrier that stops the current flow. This mechanism provides the off-state of the switch. The band-to-band impact ionization mechanism supplies electrons from the right-hand-side contact [21]. In this mechanism, the optical pulse initiates the triggering by injecting electrons that are trapped and holes that reduce the barrier at the left-hand side. The reduced barrier allows the flow of current that starts injection at the right-hand side.

Figure 2 shows the temporal evolution of the current. During the initial stage, transient current flows after the application of a large electrical potential of 110 V (550 kV/cm). The

contribution of injected electrons leads to a slight rise in the current. However, the field from the acceptor traps at the left-hand side halts this current flow. At time $t = 10^{-8}$ s, the optical pulse is applied. The photoconductivity causes a steady increase in the current. In this calculation, the electron and hole densities reach unphysical values because the growth has no Auger mechanism.

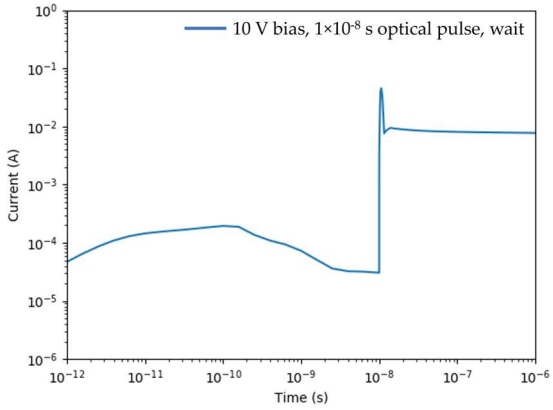

Figure 2. Time-evolution calculation of *n-i-n* device current in the dark ($t < 10^8$ s) and after an instantaneous light pulse ($t > 10^8$ s).

Figure 3 shows the spatial variation in the conduction and valence bands caused by the applied potential. This figure reveals that the band bending is very abrupt at the right-hand side. The band bending at the timestep immediately prior to the growth of current is shown in Figure 2. This figure shows that the voltage has a large variation at the right-hand side. In other words, the electric field is modest except at the right-hand side. The change in potential at the right-hand side is enabled by the applied electric potential. However, the field is provided by the electron charged defects. This result suggests that the average field will be modest outside of a few hundred nm near the biased switch electrode.

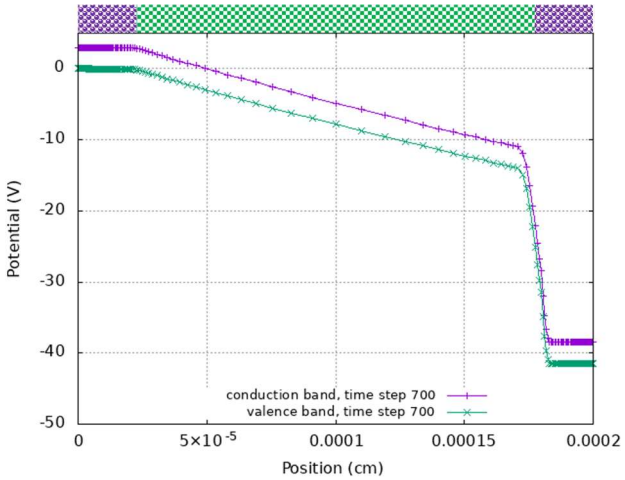

Figure 3. Computed band diagram of GaN *n-i-n* structure at the last computed time increment before the optical pulse (shown in Figure 2), varying from the left-hand contact (0) and right-hand contact (0.0002 cm). The i region is noted at the top center in green and the n region at the top sides in purple (color online).

The defect mechanism provides a field that is somewhat independent of the external circuit. Instead, it is a field created by the optically injected electrons. Once the threshold is exceeded, the carrier growth is not controlled by the circuit. However, the field provided by the circuit causes a modest carrier drift contribution to the current.

e Discussion: GaN PCSS

Additional calculations using a capacitive source (an important circuit element for applications as described in Sections 7 and 8) lead to new insights about these calculations. In both the calculation and measurement of a fabricated PCSS pulse-charged by a capacitive circuit, both the current and the switch voltage decrease as the capacitor discharges. After approximately 4×10^{-7} s, the current becomes very small, but the voltage remains constant. That voltage is defined as the lock-on voltage. This use of the term lock-on differs from the previous usage for GaAs switches. In experiments on those switches, the voltage during the on-state remained approximately constant. This constant voltage corresponds to a field of approximately 4 kV/cm, the lock-on field.

New calculations using a capacitive current source were performed to obtain insight into the ways in which behavior may diverge. Incorporating a capacitive source of charge rather than a constant one results in the current–voltage behavior shown in Figure 4. This figure shows current and voltage after optical triggering.

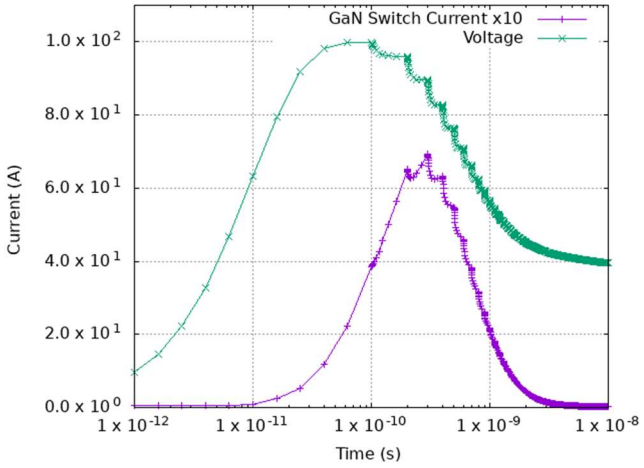

Figure 4. Calculated current–voltage of the *n-i-n* switch during and after optical triggering while the switch is charged by a capacitor.

The new theoretical results in Figure 4 are in qualitative agreement with the measured data of a comparable measured configuration shown in Section 7 below. In both figures, the current rises after optical triggering and then it decreases. In Figure 4, the current ceases when the capacitive current source is not able to maintain the on-state. The figure shows that the threshold voltage is approximately 40 V for this switch and capacitor combination.

The switch voltage remains large because the electrons trapped at the acceptors cause a large internal field that maintains the switch voltage at lock-on. This field enhancement has a primary role in the avalanche injection mechanism. Lock-on-like behavior in GaN has only recently been observed, and its mechanisms are accordingly less well-understood than those giving rise to the phenomenon in GaAs. Additional physical experimental and simulation work is required to understand, and therefore to engineer, the enormous potential for high-gain operation in these direct bandgap devices.

f Comparison of lock-on mechanism: GaN and GaAs

The two breakdown mechanisms thus differ substantially. The process in GaAs relies on the fact that the increase in carrier–carrier scattering upon triggering generates the high carrier density needed for filamentation. The increasing current reduces the field and this stabilizes the avalanche mechanism. The high-current-density region exists inside a filament. Outside the filament, the carriers achieve a low carrier density steady state. Both the high- and low-density regions are locally stable and co-exist for the lock-on field.

The GaN mechanism relies on a large density of charged defects at the anode that create a high field region under bias. These initially neutral defects capture electrons during the optical triggering process.

The two mechanisms result in different characteristic fields. In GaAs, the electric field is almost uniform throughout the device. However, in the GaN mechanism, the electric field is large near the anode and comparatively low elsewhere. The two mechanisms cause very different behaviors in a circuit. In both cases, the device is assumed to be a simple one-dimensional device with length L. The effects can be understood by considering a switch in a simple circuit consisting of a voltage source V_C (the capacitor), a load resistor R_L, and the switch under bias voltage V_S. During a quasi-static switch process, the relation between the slowly varying voltage contributions can be expressed as $V_C = IR_L + V_S$.

In this equation, the voltage source is a large capacitor that discharges during the operation of the switch. This simple circuit can be used to discuss the differences in the temporal evolution of GaN and GaAs. In the GaAs mechanism, the electric field E_{LO} during lock-on is approximately constant. Because the field is constant, the lock-on voltage $V_{LO} = E_{LO}L$ is also constant, i.e., the lock-on voltage is the switch voltage. Initially, the capacitor voltage V_C exceeds the lock-on voltage. However, at the end, when the capacitor discharges to approximately V_{LO}, the current collapses and the switch opens at $V_C = V_{LO}$.

In the case of the GaN switch, the circuit is identical. However, in this case, the field varies within the switch. It must have a large value at the right-hand side (of Figure 1) to induce avalanche injection. In that region, of thickness Δ, the voltage will be $V_{LO} = E_{LO}\Delta$. The field E_0 in the remainder of the device of thickness $L - \Delta$ will be much smaller, such that $V_0 = E_0(L - \Delta)$. The switch voltage is thus $V_S = V_0 + V_{LO}$. The voltage contribution can also be expressed in terms of the current and the resistance R_0 of the thicker region within the switch: $V_0 = IR_0$. Thus, $V_C = I(R_L + R_0) + V_{LO}$. Given that the load resistance will usually be small, $V_C \simeq V_S = IR_0 + V_{LO}$. This expression states that the switch voltage will be approximately equal to the source voltage. Furthermore, as the current approaches zero, $V_C \to V_{LO}$.

Comparing the GaAs and GaN cases reveals that the result is the same in both cases. The distinction is that the switch voltage is always the lock-on voltage for GaAs switches, but it is initially the capacitor voltage for the GaN devices.

3. SiC PCSS Devices

SiC has been widely utilized as a fundamental material for high-power, high-temperature, and high-frequency applications, owing to its outstanding electronic and thermal properties, as well as its commercial availability. When compared to first-generation semiconductor materials such as silicon (Si) and second-generation materials like gallium arsenide (GaAs), SiC demonstrates several advantages. These include a wide bandgap energy (3.0 eV for 6H-SiC and 3.2 eV for 4H-SiC), a high critical breakdown field, and superior thermal conductivity (4.9 W/cm·K for 6H-SiC and 3.7 W/cm·K for 4H-SiC). Additionally, SiC exhibits high electron saturation velocities ($1.5{\cdot}10^7$ cm/s for 6H-SiC and $1.9{\cdot}10^7$ cm/s for 4H-SiC), a low dielectric constant, and exceptional thermal stability, with breakdown fields ranging from 3 to 5 MV/cm [4,22–24]. SiC is available in numerous polytypes, including 3C, 2H, 4H, and 6H, each defined by the specific stacking order of Si-C bilayers along the c-axis of its crystal lattice. Among these, 3C-SiC is the only polytype that possesses a cubic crystal structure, while 4H-SiC and 6H-SiC both exhibit hexagonal crystal structures [25].

Numerous studies have focused on engineering the material characteristics of SiC to meet the primary requirements for high-power photoconductive semiconductor switches (PCSSs). Various growth techniques, such as undoped Lely [26,27], physical vapor transport

(PVT) [28], and ion-implanted epitaxial material (I^2 epi) [29], have been employed to produce high-quality SiC substrates [30]. However, during the growth process, defects such as ScC precipitates, nanopipes, micropipes, and cavities can arise, particularly when growth conditions are suboptimal. These defects can significantly degrade both the performance and stability of the resulting devices. Additionally, primary impurities, including N and B, are often unintentionally introduced into the material. N acts as a shallow donor, while B serves as a shallow acceptor, enabling N and B doping to create *n*-type or *p*-type semiconductor materials with enhanced conductivity [24,31].

a. Doping considerations

Two primary approaches are available for obtaining high-quality semi-insulating (HPSI) SiC. The first approach involves refining the SiC growth process to minimize the unintentional incorporation of N and B impurities, thereby achieving high purity SiC. Alternatively, a compensating third dopant, such as V or Ti, may be introduced to balance the excess N donors or B acceptors [29,30]. For example, when SiC is doped with V to form V-compensated semi-insulating (VCSI) SiC, the dopant acts similarly to the Z_1/Z_2 defect centers found in HPSI SiC. V has three charge states and forms two energy levels within the bandgap as an amphoteric dopant. Neutral V (V_N) can capture an electron (or emit a hole) to become an acceptor (V_A^-), or emit an electron (or capture a hole) to become a donor (V_D^+). The acceptor level corresponds to the transition between V_N and V_A, often referred to as the shallow donor deep acceptor (SDDA), while the donor level corresponds to the transition between V_N and V_A, known as the deep donor shallow acceptor (DDSA). V effectively compensates *n*- or *p*-type doping and pins the Fermi level near the mid-gap, leading to a high dark resistivity (>10^9 Ω·cm). Furthermore, V acts as a recombination center and has been demonstrated to influence the control of carrier lifetime, further enhancing the performance of SiC-based devices [24,30–32].

Co-doping interacts with the intrinsic behavior of V defects, making the quantification of optical transitions in SiC particularly challenging. V functions as an amphoteric dopant in SiC, with two energy levels emerging within the bandgap as it transitions between three distinct charge states. The acceptor level ($0/-$ transition) arises when the neutral V accepts an additional electron, for instance, from an ionized donor, becoming negatively charged. Conversely, the donor level ($0/+$ transition) is observed when the neutral vanadium state donates an electron, becoming positively charged. The acceptor level is consistently positioned higher in energy relative to the valence band. Figure 5 illustrates the band diagram for SiC, where the two transition levels are represented by horizontal black lines, and the three charge states are shown as discrete vertical columns. Additionally, the figure depicts scenarios involving co-doping with either donors or acceptors. The photogeneration pathways in Figure 5 are represented by diagonal arrows indicating transitions between different energy levels [24,32]. When V is the sole dopant in SiC (left diagram), it resides in its neutral charge state, allowing photogeneration transitions to both negative and positive charge states, as indicated by the green arrows. The transition to the negative charge state is accompanied by a dashed arrow, representing the generation of a hole in the valence band, while an electron is promoted from the valence band to the acceptor level.

In the case where V is compensated by shallow donors such as N (Figure 5b), it resides in the negative charge state due to an electron transition to a lower energy state (red arrow) and can return to its neutral state only through electron emission (green arrow). When V is compensated by shallow acceptors such as Al or B (Figure 5c), it remains in the positive charge state due to electron transition to a lower energy state (red arrow) and can only return to its neutral state by emitting a hole (green arrow). The processes of hole generation and annihilation are again denoted by dashed arrows. This behavior is further complicated by the fact that V, like most transition metals, retains some of its atomistic properties in the

form of excited atomic states, even when embedded in a host lattice. During illumination, these states create additional transition pathways, as indicated by the orange arrows. These pathways can be detected in the absorption spectrum but are not believed to generate a photocurrent [29,30,32–35].

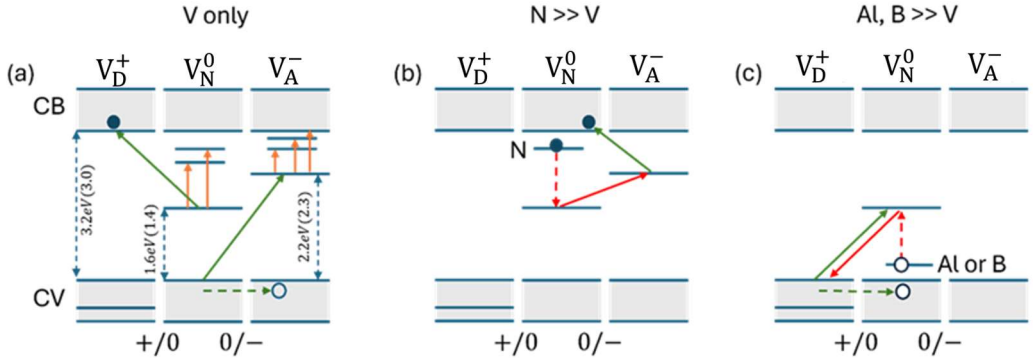

Figure 5. Band diagrams of SiC:V showing the occupancy of the different V states depending on the presence of other co-dopants and the energy levels needed to transit between these states. The provided energy values are for the 4H polytype whereas their equivalences for the 6H polytype are shown in parentheses. Carrier generating transitions are shown in green, noncarrier generating (or parasitic) transitions are shown in yellow, and transitions of carriers from co-dopants to V levels are shown in red. (**a**) is the case of SiC:V without co-dopants where carriers can be generated only from the neutral V_N state. (**b**) is the extreme case of N ≫ V, where all V is converted into the acceptor V_A state allowing only electron generation from this state into the conduction band. (**c**) is the opposite case, where Al or B ≫ V and all V is converted into the donor state allowing only hole generation from this state into the valence band (re-generated from Ref. [32]).

b Switch geometries

Various SiC PCSS structures [36] have been proposed to address challenges related to breakdown voltage thresholds, on-state resistance, and conversion efficiency. Typically, these devices are categorized into two structural types: lateral, where both electrodes are positioned on the same plane, and vertical, where the electrodes are located on opposite planes [33]. Table 2 compares the most important characteristics of 4H and 6H SiC PCSS designs. Lateral devices, which often use low-impurity SiC polytypes, generally rely on above-bandgap wavelengths to trigger the switches, as this enables maximum carrier collection through intrinsic absorption near the surface, where a strong electric field is present. Conductivity modulation in this surface region shows promises for achieving a substantial on/off resistance ratio, leading to high output currents [34].

However, when the switch is triggered by a high-power laser pulse, gas ionization may occur at the surface, generating positively and negatively charged ions. These ions are subsequently accelerated by the electric field, initiating an avalanche multiplication effect that forms a discharge channel, eventually resulting in a surface flashover (in SiC, as in GaN, this has been confused with lock-on). To mitigate surface breakdown issues, rear-illuminated devices with radial structures (as shown in Figure 6b) have been developed. These structures have been shown to increase blocking voltages by up to five times by reducing point peak currents at the metal/SiC interfaces, thereby enhancing device reliability [4,35].

SiC PCSSs with vertical structures have been developed with side illumination (as shown in Figure 6c) that exploit the bulk material's extrinsic absorption of below-bandgap wavelengths. Innovative illumination techniques such as silver back contact mirrors [37] and twisters [38] have been developed to enhance photon absorption uniformity in thick bulk substrates. Transparent conductive oxide (TCO) electrodes, such as aluminum-doped zinc oxide (AZO) [39] and indium tin oxide (ITO), have enabled front and backside exci-

tation (Figure 6d). Vertical structures provide practical solutions for mitigating surface flashover and handling high current densities [40]. However, achieving high-quality transparent electrodes with low resistance and minimal absorption has posed significant challenges due to their complex composition and intricate fabrication processes. Surface roughness and internal defects in TCO materials can negatively impact reflection, absorption, and transmission, ultimately diminishing the device's overall performance.

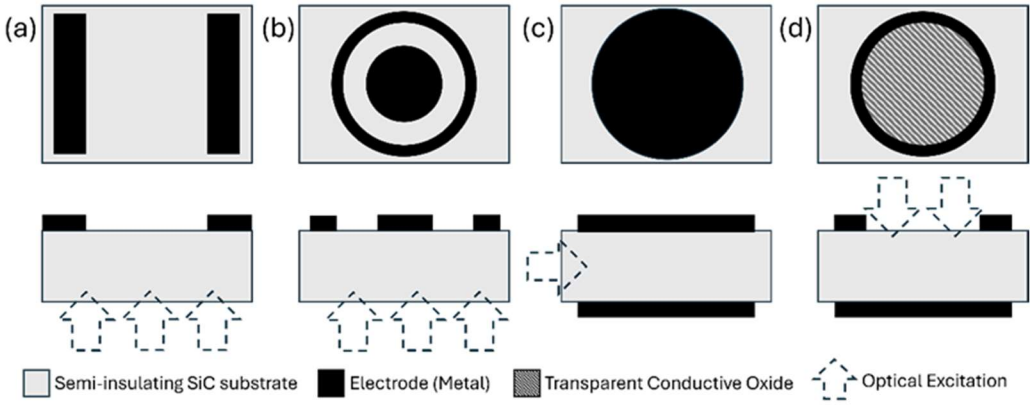

Figure 6. Common designs for PCSS devices used in high-power microwave (HPM) applications (top view (top) and cross-section (bottom)): (**a**) lateral in-line contact, (**b**) lateral radial, (**c**) vertical PCSS design with top–bottom metal contacts with side illumination, and (**d**) vertical structure with top–bottom transparent conductive oxide (TCO) with front-rear excitation.

More critically, TCO degradation originating from defects may be a primary cause of PCSS breakdown during high-fluence laser experiments. The pulsed laser used to illuminate the surface interacts with the transparent electrode, resulting in the formation of numerous bubbles at the side of the electrode that directly contact the air under bias voltage. As Joule heating and laser heating accumulate, the transparent electrode absorbs heat up to a critical threshold, leading to gradual melting and vaporization. This process forms localized hot spots at the SiC/TCO–air interface. When the laser directly impacts the substrate, damage within the substrate accumulates over time, eventually creating breakdown channels. As this damage worsens, the device ultimately fails. A vertical structured 6H-SiC:V could accumulate ~200 pulses at charge voltages ranging from 15 to 17 kV and 300 to 400 pulses with currents in excess of 1 kA without any discernable damage, or degradation in performance [39,40]. These approximate field and current density values compare unfavorably with GaAs switches, but favorably with GaN switches in comparable geometries.

Table 2. Survey of state-of-the-art values for SiC:V PCSS device electrical properties observed in the literature.

Ref.	Material	Structure	Wavelength	P_{laser}	$V_{blocking}$	$V_{op.}$	I_{out}	R_{on}	R_{off}
[40]	6H-SiC:V	Vertical	532 nm	530 kW	>150 kV/cm	20 kV	50 A	244 Ω	
[37]	4H-SiC:V	Vertical	532 nm	18.2 MW/cm^2	260 kV/cm	12 kV	840 A	7.5 Ω	
[41]	6H-SiC:V	Vertical	532 nm	31.2 mJ, 17 ns	225 kV/cm	20 kV	500 A	5.6 Ω	10^{11} Ω
[4]	4H-SiC:V	Lateral	355 nm	1 mJ, 7 ns	370 kV/cm	26 kV	450 A	2 Ω	
[36]	6H-SiC:V	Vertical	532 nm	4 MW		17 kV	1500 A	<1 Ω	2×10^{10} Ω
[39]	4H-SiC:V	Vertical	532 nm	100 kW	200 kV/cm	20 kV	100 A		10^{12} Ω
[34]	4H:SiC:V	Lateral	355 nm	0.5 mJ, 7 ns	231 kV/cm	12.4 kV	182 A	12 Ω	4×10^{12} Ω
[34]	4H:SiC:V	Radial	355 nm	0.5 mJ, 7 ns	178 kV/cm	32.2 kV	938 A	8 Ω	12×10^{12} Ω
[24]	6H:SiC:V	Vertical	532 nm	13 mJ	27.4 MV/m	11 kV	150 A	2 Ω	10^{12} Ω

SiC PCSSs have been able to achieve either high-voltage operation or high-current operation but have had difficulty achieving both simultaneously with long device lifetimes. In addition, PCSSs operated at high electric fields (>100 kV/cm) have required pulse charging circuits due to high power dissipation in the off-state. Although intrinsic PCSSs are more efficient than extrinsic PCSSs, both devices when operated in the linear mode currently require large amounts of laser energy to achieve low on-state resistances. This subsequently requires large high-power lasers be used to trigger the PCSSs. Therefore, ultrawide bandgap (UWBG) materials with higher thermal conductivity and critical strength field characteristics continue to be investigated.

4. Diamond PCSS Devices

Diamond's exceptional physical properties make it an ideal semiconductor material for PCSSs, particularly for high-voltage and high-power switching applications due to its very high thermal conductivity [42]. As a UWBG semiconductor, diamond possesses a bandgap of 5.5 eV. Intrinsic diamond demonstrates a high critical electric field (10–20 MV/cm), high carrier mobility (up to 2100 $cm^2/V{\cdot}s$ for holes and 1060 $cm^2/V{\cdot}s$ for electrons), and excellent thermal conductivity (22–24 W/cm·K) [35–38]. Both intrinsic [43] and extrinsic [44] diamond PCSSs have been studied, utilizing excitation wavelengths either above or below the diamond bandgap, respectively. Previous research has observed photoconductivity in intrinsic diamond using UV-band excimer lasers under high electric fields of up to 0.7 MV/cm [45,46]. In contrast to intrinsic diamond PCSS devices, which rely on photon energies above the bandgap (band-to-band excitation), typically requiring UV wavelengths below 226 nm, extrinsic PCSSs operate with sub-bandgap photon energies, where carriers are excited from dopant or defect levels. This allows diamond devices to function using more accessible visible or infrared wavelengths, while retaining the advantageous properties of diamond. N-doped diamond has been identified as a promising candidate for extrinsic PCSS applications, particularly in vertical structures, due to its high photoresponsivity to sub-bandgap excitation (a direct parallel with SiC:V and GaN:Mn).

The implementation of diamond PCSSs requires precise control over carrier generation, which dictates the wavelength and power of the input optical source, and carrier recombination, which determines the achievable switching frequency. This, in turn, requires the precise control of material quality and doping profiles. The manufacturing of high-quality synthetic diamond with controlled defect concentrations, however, remains a complex process. Furthermore, the available substrates tend to be relatively small and challenging to process. High-purity single-crystal diamond is generally unsuitable for PCSS applications due to its µs-scale carrier lifetimes [47]. To overcome this limitation, extrinsic photoconductivity, where defects or impurities modulate generation and recombination, is utilized to reduce carrier lifetimes [48,49]. Polycrystalline diamond PCSSs with picosecond response times have been demonstrated, but the exact nature of deep traps remains unclear, complicating the development of practical devices. Furthermore, switching impedance achieved to-date has been higher than many commercial loads, being generally not less than hundreds of Ω [45]. The technological immaturity of diamond as a semiconducting medium, very low gain, and high switching impedance, make it unsuitable at present for integration into commercially relevant loads. While promising based on intrinsic material properties, it requires advances in the knowledge of impurity levels and carrier dynamics to be commercially viable.

Impurities enable the use of extrinsic photoconductivity, as demonstrated with SiC:V. In diamond, N typically acts as a single-substitutional impurity, creating a deep donor level approximately 1.7 eV below the conduction band, which can be accessed through sub-bandgap excitation [50]. This deep donor level, along with a large carrier capture cross-

section, allows N-doped diamond to exhibit sub-nanosecond carrier lifetimes. Natural diamond PCSS devices have demonstrated lifetimes in the range of 0.5 to 1 ns [43,51]; however, the N concentrations in these natural diamonds were limited (Figure 7a) [52–54]. As a result, synthetic diamond, with higher levels of incorporated N, has emerged as an attractive alternative for PCSS applications.

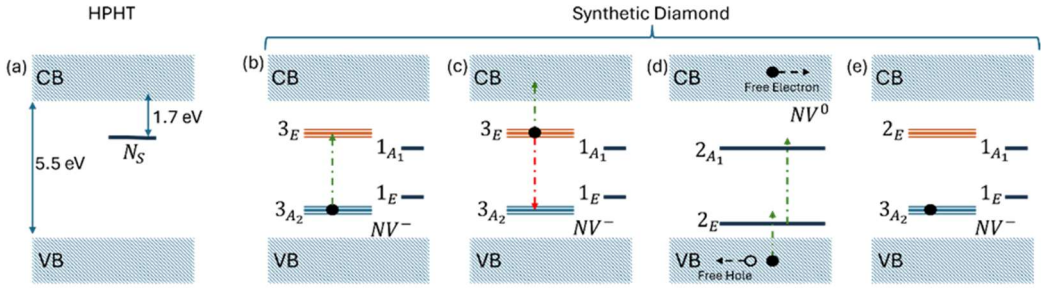

Figure 7. A simplified electronic energy level diagram (not to scale) represents (**a**) the energy states in HPHT diamond and (**b**–**e**) the V_N^- center at room temperature. In (**b**), the absorption of a first photon excites an electron from the $^3A_2$ ground state to the 3_E excited state of the V_N^- center. In (**c**), ^3E electrons can either radiatively decay back to the $^3A_2$ ground state or be further excited into the diamond conduction band (CB) by absorbing a second photon. The spin-selective non-radiative decay of electrons to the singlet state $^1A_1$ (transition 3), followed by a transition to the metastable ^1E state, enables photo-detected magnetic resonance (PDMR) and optically detected magnetic resonance (ODMR). In (**d**), the two-photon ionization of the V_N center results in the formation of an V_N^0 center and a free electron in the CB. Through a subsequent two-photon process, in which the V_N^0 center is first excited and then an electron from the valence band (VB) is promoted into the vacated orbital of the V_N^0 center, (**e**) the V_N center can be converted back to its negatively charged state (V_N^-) (re-generated from Ref. [54]).

The mechanism underlying the photoelectrical detection of V_N centers can be explained by a two-photon ionization process, as depicted in Figure 7b. Initially, an electron in the triplet ground state of $^3A_2$ in the V_N center is excited to the triplet excited state ^3E by absorbing the first photon. Subsequently, a second photon ionizes the electron into the conduction band, causing a charge state conversion from negatively charged V_N centers (V_N^-) to neutral V_N centers (V_N^0). In the third step, an electron in the V_N^0 state is excited from the ^2E to the $^2A_1$ level, and finally, an electron is excited from the valence band to the vacant state of V_N^0, reverting the charge state back to V_N^- as described in Refs. [28,52,54]. The free electrons and holes generated during the photoionization process contribute to the photocurrent, enabling continuous photocurrent detection. Interestingly, under higher illumination, the increase in photocurrent exhibited a linear trend rather than a quadratic one. This behavior could be attributed to two potential factors: the saturation of the transition from $^3A_2$ to ^3E, and background signals arising from other defects, such as isolated substitutional N atoms, also known as P1 centers.

An investigation into three grades of synthetic diamond [52]—high-pressure high-temperature (HPHT) belt-press, HPHT split-sphere, and chemical vapor deposition (CVD) general—revealed that N impurities can act as efficient recombination centers, leading to sub-ns response times. The HPHT Belt-Press diamond PCSS demonstrated responsivity at 532 nm in the range of 2–7 $\times$ 10^{-5} A/W under a moderate electric field of 2 kV/cm. In comparison, Schottky diode diamond photoconductive detectors exhibited a responsivity of only 10^{-6} A/W at a few volts of reverse bias, with response times no faster than 100 ns. Non-epitaxial single-crystal diamond detectors, biased at 50 V, were unable to achieve responsivity greater than 10^{-7} A/W in the visible spectrum without the use of defect passivation treatments. Natural diamond PCSS devices, biased at 7 kV/cm, achieved a responsivity of 5 $\times$ 10^{-4} A/W at an above-bandgap wavelength of 222 nm. For comparison,

a GaN PCSS biased at 24.5 kV/cm demonstrated a responsivity of 3.5×10^{-5} A/W at 532 nm with 2 mJ/pulse, while a SiC PCSS, biased at 18.7 kV/cm, achieved a responsivity of 2.5×10^{-5} A/W at 532 nm with 4 mJ/pulse.

To gain a deeper understanding of the characteristics of synthesized diamond for high-power optoelectrical applications, various diamond structures for extrinsic PCSSs were explored [45]. These structures included an insulating high-pressure high-temperature (HPHT) type Ib substrate (highly N-doped), a chemical vapor deposited (CVD) type IIa substrate (unintentionally doped), and a CVD-grown semiconducting B-doped epilayer on a type IIa substrate, as well as B-implanted type Ib and IIa substrates. Significant extrinsic photoconductivity, characterized by a large on/off current ratio, was demonstrated in both highly N-doped type Ib diamond and unintentionally doped type IIa single-crystalline diamond using below-bandgap visible excitation at 532 nm. In contrast, photoconductivity in response to lower-energy 1064 nm excitation was only observed in B-doped diamond. The photoresponse in insulating Ib and IIa diamond substrates was believed to be facilitated by carrier photogeneration at the contact edges, combined with the photoionization of substitutional nitrogen, which reduced the resistivity of the diamond. The on/off current ratio of the type Ib device reached values on the order of 10^{11}. Furthermore, the effects of dopant compensation between B and N in diamond were observed in three distinct ways: (1) reduced dark currents in devices on B-implanted Ib versus IIa substrates, (2) diminished photoresponses in devices on B-implanted versus unimplanted Ib substrates, and (3) the presence of a photoresponse to 1064 nm in devices on B-implanted IIa substrates, which was absent in those on B-implanted Ib substrates.

A recent study demonstrated a 130 mA/W intrinsic responsivity (for wavelengths below 226 nm) using a buried, metallic heavily doped (p^+) current channel within an HPSI diamond as the active absorption layer. The lateral PCSS devices exhibited high on/off ratios (>10^{11}), fast rise and fall times (~2 ns), and impressive current densities of up to 44 A/cm^2. Additionally, these devices showed linear current–voltage characteristics up to a DC bias of $\pm$60 V, suggesting that even higher current densities could be achieved before reaching carrier velocity saturation [42]. Future studies could focus on optimizing the switch design to enhance photon absorption. The development of transparent or buried contacts could provide solutions to reduce both contact resistance and diamond resistivity under photoexcitation, without contributing to an increase in dark current.

5. β-Ga_2O_3 PCSS Devices

B-Ga_2O_3 (gallium oxide), like diamond, is an emerging UWBG material with great promise in PCSS applications. In addition to a bandgap and critical field of 4.8 eV and critical field strength of ~6 MV/cm, it has the additional advantage of its potential for cost-effective, large-scale production through methods such as edge-defined film-fed growth (EFG) [55–58].

In β-Ga_2O_3, the Fe acceptor is positioned about 0.7–0.8 eV below the conduction band (CB). This acceptor can emit electrons to the CB under sub-bandgap illumination, functioning similarly to V in SiC and N in diamond. The primary defects in β-Ga_2O_3 are Si (shallow donor) and Ir (deep donor), both of which unintentionally dope the material during the growth phase. Fe is commonly used in higher concentrations, often by an order of magnitude greater than Si, in order to achieve semi-insulating characteristics in the material [56–59].

The primary optical absorption pathways are illustrated in the band diagram presented in Figure 8. It is assumed that the shallow Si donor is fully compensated by the Fe dopant, resulting in the coexistence of both Fe^{2+} and Fe^{3+} species within the sample at equilibrium. The lowest energy absorption process involves the release of an electron to the CB, thereby

converting Fe^{2+} to Fe^{3+} (Path I in Figure 8) [58,60]. Although the Fe^{2+} level is positioned approximately 0.7–0.8 eV below the CB, experimental observations have indicated that absorption levels can extend to 1.2–1.5 eV below the CB for this trap. This extension is attributed to the relaxation energy within the lattice, with similar energetic behaviors predicted for Fe residing in both the tetrahedral and octahedral Ga sites. Consequently, the 1.17 eV optical energy associated with 1064 nm light results in only minimal transmission to the CB. Higher-energy optical sources, tested at 2.3 eV and above, have been found capable of activating absorption in the deep Ir^{3+} state, as well as other deep donors and acceptors that may be present [61]. Since Ir^{3+} functions as a deep donor, its absorption of photons with energies of 2.3 eV or higher leads to two possible pathways: direct electron emission to the CB (Path II in Figure 8) or a charge-transfer transition to Fe^{3+} or potentially another defect (Path III in Figure 8) [62,63].

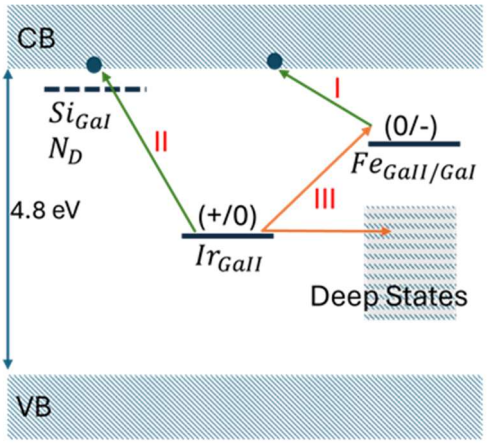

Figure 8. β-Ga_2O_3:Fe trap model with active impurities in the sample. Green arrows correspond to carrier generation and orange arrows correspond to internal transitions (re-generated from Ref. [61]).

Additionally, optical absorption peaks related to Fe in β-Ga_2O_3 have been observed around 2.2 eV, with the absorption decreasing at higher energy levels. This suggests that Fe^{2+} emission is more pronounced in the 2.3–2.7 eV range (corresponding to green and blue light) compared to higher-energy excitation sources [64]. The first demonstration of Fe-doped β-Ga_2O_3 [61] as a PCSS has confirmed its ultra-high breakdown field of greater than 2 MV/cm and a free carrier recombination lifetime of less than 100 ps; however, its room-temperature gain is 100–1000× poorer than state-of-the-art devices fabricated from diamond, GaN, and SiC. With an understanding of the trapping and carrier transport of deep states in β-Ga_2O_3 still at an early stage [63], the material is not yet competitive with more mature material systems as a switching medium. These characteristics strongly position it as a promising candidate for next-generation high-power and ultra-fast switches, particularly in extreme environments [59,60,62,65].

6. GaAs PCSS Devices

GaAs is among the earliest materials to be investigated as a PCSS substrate due to its early technological maturity, with research into GaAs switches commencing in the early 1980s, shortly after the first Si PCSS in 1975 [66]. It continues to justify research due to its very high crystalline quality, ability to be grown from a melt (by vertical gradient freeze and modified Czochralski techniques), high dielectric strength, and direct bandgap [67–69]. These properties enable devices with picosecond rise times and high breakdown fields despite its narrow (1.4 eV) bandgap (due to the ability to grow very thick films economically). Its direct bandgap makes it a much more efficient optical absorbing medium than Si or SiC, alleviating triggering requirements. It is also one of only three materials to have exhibited a high-gain

mode (separate effects referred to collectively as lock-on). Early work to extend switching lifespan to >10^4 shots increased both the optical power and trigger system complexity [70], primarily by seeding large numbers of current filaments in vertical devices, as pictured in Figure 9 [5,71,72].

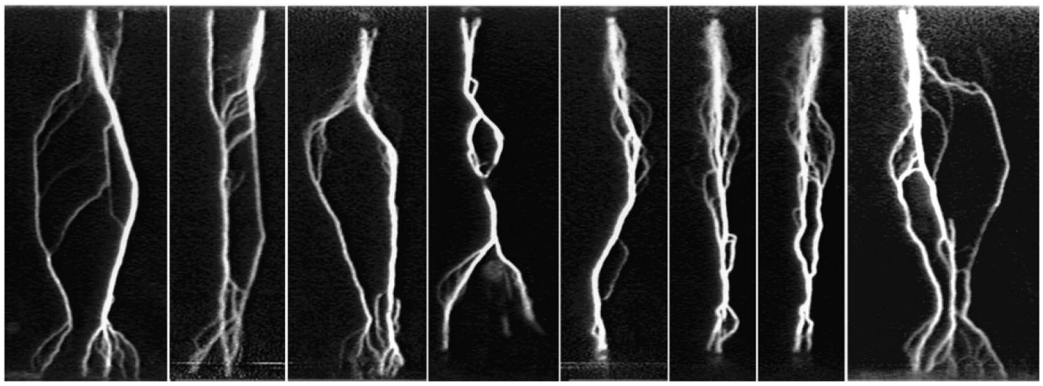

Figure 9. Camera images of filamentary conduction through the bulk of GaAs switches taken during lock-on events (reproduced from Ref. [73]).

Lock-on in a GaAs PCSS device was observed first by Zutavern and coworkers at Sandia National Laboratories in 1987 [74,75]. It was the first optically triggered latching behavior observed in a semiconductor switch (functionally comparable to latching in silicon-controlled rectifiers), generating ~10^5 electron–hole pairs per trigger photon [5]. The observation of optical emission from current filaments propagating from the location of the laser trigger between the two electrodes is ubiquitous in lock-on mode, and is not observed during linear-mode operation, leading to the basis for claims of lock-on (distinct from surface flashover or breakdown) in other materials.

GaAs has the drawback of poor durability due to low electrical and optical damage thresholds. Accordingly, the careful design of the optical trigger, including line-emitting lasers, optical beam splitters, and electrode design for large numbers of filaments, is required to achieve high power without damaging the device [71,72]. These factors have limited production to specialized research applications, including pulse and kHz amplifiers [76,77].

7. (Al)GaN PCSS Devices

GaN is a semiconductor now entering technological maturity that is well-suited to realize the promise of ultra-low jitter PCSS devices due to its high saturation drift velocity, large and direct bandgap, radiation hardness, high-temperature operability, and high field strength [78]. Triggering in linear mode has been demonstrated with intrinsic and extrinsic light sources [79], and nonlinear operation has been recently observed [6]. While early reports of GaN PCSS devices, especially vertical designs, suffered from low breakdown fields, reports utilizing recently available free-standing material achieve near-ideal breakdown values up to 1.6 MV/cm [80,81].

The related binary and ternary UWBG compounds AlN and $Al_xGa_{1-x}N$ offer similar promise to GaN as a PCSS medium. Photoconductive switching has not been demonstrated to date in either material, in large part because bulk (freestanding), low-dislocation density material has only recently become available. PVT or hydride vapor-phase epitaxy (HVPE) is used to develop freestanding, high-quality AlN; however, the same technique cannot readily be used to grow freestanding AlGaN due to the added complexity of achieving a uniform composition of the ternary [82,83].

SiC is generally the best-understood and most widely studied of the PCSS media. It has high thermal conductivity and its bandgap makes it well-suited to intrinsic trigger-

ing by conventional lasers, and doping with V can enable extrinsic triggering at visible wavelengths [24]. SiC, however, typically has higher leakage current than GaAs and lower saturation drift velocity than GaN [69]. No regime of negative differential resistance has been identified in SiC, suggesting a regime of nonlinear conduction may also not exist. If this is the case, triggering requirements must scale in power linearly with switch current-handling requirements. The direct, narrow bandgap and high dielectric strength of GaAs make it efficiently triggerable with very high slew rate [69] in linear and nonlinear regimes [5]. Its shot life, however, is typically limited to hundreds of shots and its relatively low optical damage threshold limits trigger intensity [71,84,85].

Recent collaborative efforts between Sandia National Laboratories and the University of New Mexico have advanced the state-of-the-art in PCSS implementation for both material development and circuit integration through the ARPA-E BREAKERS program [86–88], among others. A medium-voltage (6 kV) DC circuit breaker was chosen as a PCSS demonstration vehicle composed of a normally-on leg assembled from cascaded SiC junction field-effect transistors (JFETs) and a normally-off leg based on a GaN PCSS [88]. This implementation has the advantage of providing (1) a grid-integrable power handling capability utilizing the GaN PCSS, and (2) an example of clear complementarity between SiC and GaN.

a. PCSS fabrication

Two considerations primarily motivate the selection of dopant: the need for high resistivity, and the desirable characteristic of efficient sub-bandgap optical absorption. The former is necessary for suppressing leakage current in the off-state, and the latter for enabling triggering with compact visible or IR light sources. Mn and Fe are the two most technologically mature GaN doping species known to have very deep ionization states near the mid-gap [20,89], making them favorable candidates for extrinsically triggered PCSS fabrication. The dopants reported to have been used to produce SI-GaN for PCSSs (Mn and Fe) are shown in the context of other potential, but untested, dopants in Figure 10. The deep traps introduced by V (VB + 1.39/2.07 eV), Cr (VB + 2.44/3.07 eV), Mn (VB + 1.46/1.61 eV), Fe (VB + 0.71/2.80 eV), and Co (VB + 0.88/1.54 eV) have the potential to facilitate the trap-assisted avalanche multiplication believed to be required for lock-on in GaN. High-quality free-standing GaN:Fe and GaN:Mn (dopant concentration near 10^{19} cm^{-3}) substrates are grown either ammonothermally or by HVPE to a thickness of ~300 μm by commercial vendors.

Switches are fabricated in both lateral and vertical geometries. Lateral switches are fabricated using rectangular Ti/Al/Ni/Au contacts separated by between 0.6 and 3 mm. Vertical switches are fabricated using identical metallization on the front and back (Ga- and N-face) of the material coaxially. Circular grid anodes were designed for linear mode operation (to maximize the uniformity of illumination during triggering) or a very-low-fill factor hole grid was designed for nonlinear mode operation (to enable optical seeding of current filaments during triggering). Optical micrographs of these geometries are shown in Figure 11.

The GaN PCSS devices were constructed as unipolar two-contact devices with a lateral geometry and doped uniformly with either Mn or Fe to achieve a resistivity of 10^{9}–10^{14} Ω·cm. This doping scheme has the benefit of allowing extrinsic triggering by the creation of a large number of deep traps [24] which, in turn, allows triggering from the backside as well as the front. The switches were biased up to 40 kV/cm (2 kV) and triggered by a 5 ns pulsed laser focused on the GaN surface between the contacts. The laser wavelength was varied from 650 to 1050 nm in 100 nm increments to better understand the reliability of switching and photoresponsivity. To interrogate nonlinear switching behavior, luminescence associated with switching events was monitored with separate cameras monitoring visible and infrared wavelengths to distinguish laser light reflected from the

sample surface, light emitted from surface filaments, and current filamentation within the GaN bulk.

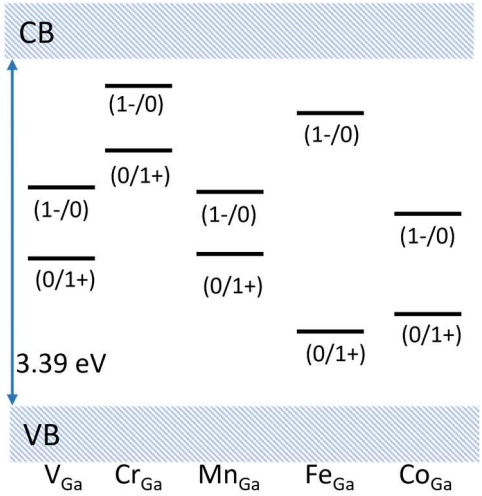

Figure 10. Predicted electronic structure and deep defect levels for magnetic 3D dopants in cubic GaN. All of the 3D dopants are energetically favored to substitute in the Ga sublattice. The first two transitions for V (VB + 1.39/2.07 eV), Cr (VB + 2.44/3.07 eV), Mn (VB + 1.46/1.61 eV), Fe (VB + 0.71/2.80 eV), and Co (VB + 0.88/1.54 eV) are illustrated schematically within the room-temperature GaN bandgap (re-generated from Ref. [20]).

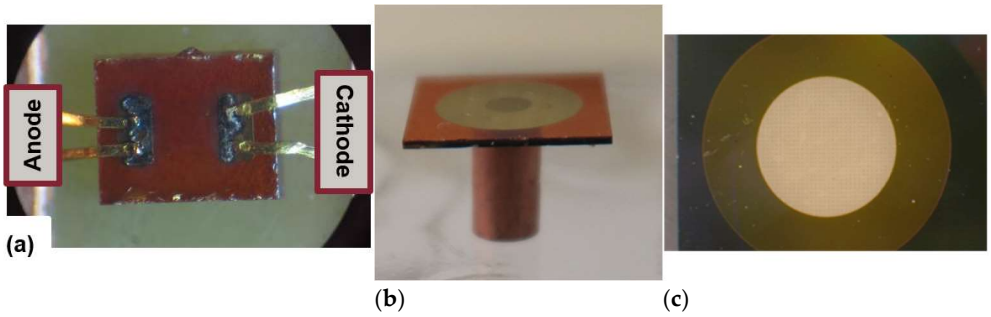

Figure 11. Optical micrographs of fabricated GaN:Mn PCSS devices in (**a**) lateral geometry, (**b**) vertical geometry with coaxial heat-sink, and (**c**) plan view of high-hole-density anode {center} and circular backside cathode {outer circle}.

b PCSS performance

Switching jitter is found to be inversely proportional to field, as illustrated in Figure 12. To achieve the promise of ps-scale jitter in Mn-doped GaN switches, field strengths of >40 kV/cm are needed. The doping species is also found to play a significant role in switching performance, as shown in Table 3. While a delay between laser triggering and closing of the switch exists for all devices, this is both larger and more variable in Fe-doped samples. Delay during the successful triggering of GaN:Fe switches was significantly longer than for the GaN:Mn devices, suggesting lower photo-carrier generation rates in Mn-doped devices compared with Fe-doped devices at this trigger wavelength of 800 nm.

Below 25 kV/cm and 22.5 μJ of laser pulse energy at λ = 800 nm, the switch operates in the linear mode; however, when the field and pulse energy exceed these values, a nonlinear switching mode is observed (see Figures 13 and 14a). These switching events are confirmed both in air (where surface flashover occasionally occurs) and in an atmosphere of insulating SF_6. The location and near-bandgap emission wavelength of the flashover, and the current filamentation typical of high-gain switching, are confirmed by wavelength-resolved camera images as shown in Figure 13. The energy requirement to initiate nonlinear conduction, holding field constant, also depends superlinearly on the laser trigger wavelength

(Figure 14b). While the physical mechanisms must be elucidated by further study, this result confirms a high-gain switching mode in GaN is achievable.

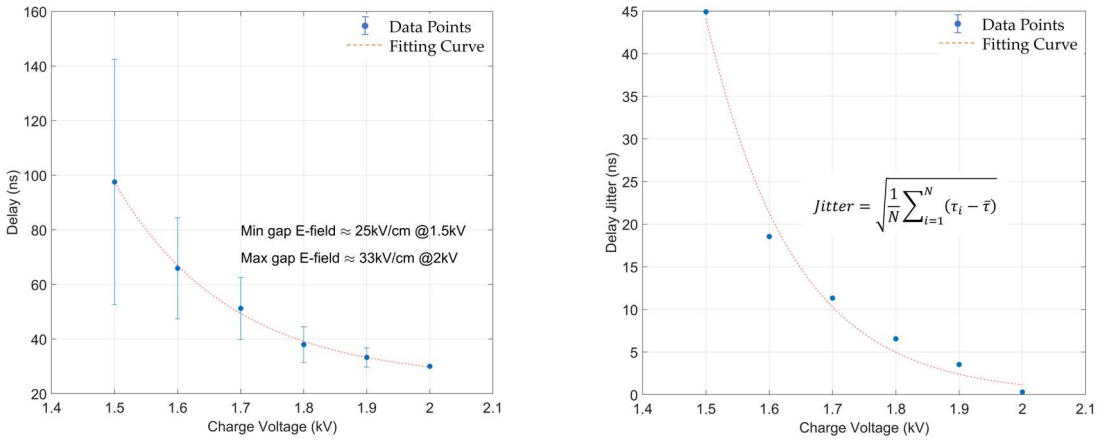

(**a**) (**b**)

Figure 12. Switching (**a**) delay and (**b**) jitter for lateral Mn-doped GaN PCSS with 600 µm gap for varying charging voltages when triggered using 20 µJ of laser energy at 800 nm.

Table 3. Laser-triggering delay for Mn- and Fe-doped GaN PCSS devices at 40 kV/cm.

Dopant	Min. Trigger Energy [µJ]	Mean Delay [ns]	Jitter [ns]	Reliability [%]
Mn	22.5	27.8	2.1	100
Fe	1500	58	12.4	35

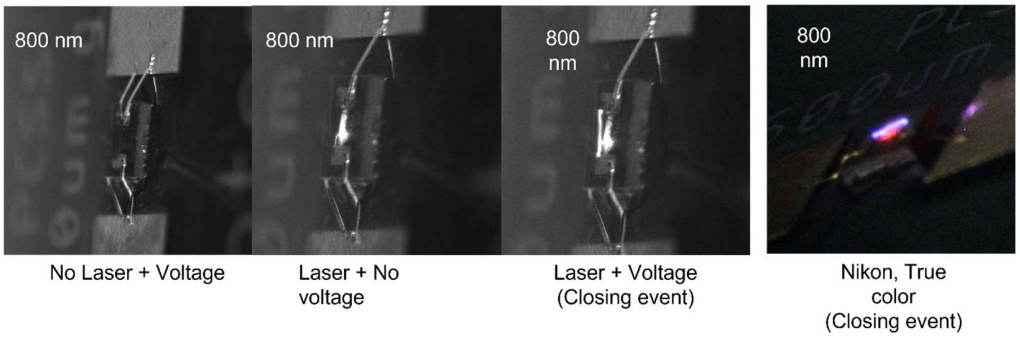

Figure 13. Optical images (black and white image taken using CCD; color image taken using a digital camera) of lateral PCSS triggered with λ = 800 nm laser.

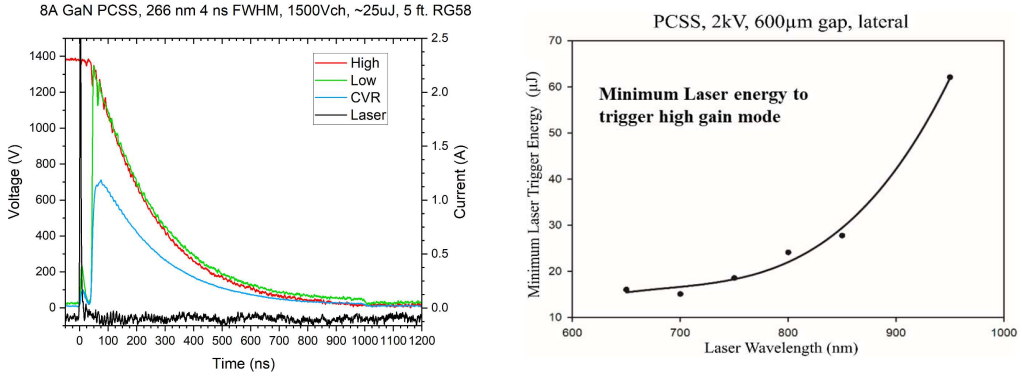

(**a**) (**b**)

Figure 14. (**a**) Current–voltage trace of non-linear triggering event of Mn-doped PCSS biased to 25 kV/cm and (**b**) laser energy required to trigger GaN PCSS into a non-linear mode as a function of laser wavelength (fit serves as a guide to the eye).

8. Application Case Study: A Medium-Voltage PCSS Breaker

Medium-voltage direct-current (MVDC) electric power, ranging from 5 kV to 65 kV, provides several advantages over alternating current (AC) systems, including reduced power losses and lighter cables [90]. Additionally, MVDC systems offer superior control and efficiency in converting electrical energy for various applications, including energy storage, renewable energy generation, and electric vehicle (EV) charging stations [91]. However, the adoption of DC systems is constrained by the need for affordable, reliable, and rapid fault detection and protection mechanisms. Unlike AC systems, which naturally experience zero current crossing, aiding fault protection, DC complicates the implementation of effective fault protection strategies [92].

Traditional mechanical circuit breakers (CBs) are hindered by slow response times, diminished reliability after repeated switching, low efficiency, and substantial size. These drawbacks can be addressed by solid-state circuit breakers (SSCBs), which leverage semiconductor devices for switching, offering significantly faster response times than mechanical CBs and minimizing energy dissipation during faults [93]. Advances in wide-bandgap (WBG) semiconductors, like silicon carbide (SiC) and gallium nitride (GaN), have outperformed silicon (Si)-based systems in efficiency and performance [88]. However, the limitation of commercially available SiC devices to 3.3 kV necessitates connecting multiple semiconductors in series for MVDC circuit breakers to enhance voltage tolerance beyond individual elements. This series operation demands precise synchronization to avoid transistor overvoltage during transitions and to maintain leakage current balance in steady state.

8.1. SSCB Topology

The system showcased in Figure 15 is the solid-state circuit breaker (SSCB) that has been proposed, designed, and demonstrated by Sandia National Laboratories [88]. This system is characterized by a high-voltage switch (HV switch), which is assembled using a series of low-voltage, normally-on SiC junction field-effect transistors (JFETs). It also incorporates an absorbing branch, composed of a capacitor (C) in series with the GaN PCSS devices described in Section 7 (forming the normally-off branch), and a metal oxide varistor (MOV) for overvoltage protection. During standard operation, the HV switch acts as the main pathway for conducting the load current (the normally-on branch). When a fault occurs, the PCSS is triggered, effectively rerouting a portion of the fault current away from the HV Switch. This strategic diversion facilitates a safe transition of the HV switch to an off-state, significantly mitigating the potential thermal stress associated with disrupting the full fault current.

Figure 16 conceptually illustrates the operational behavior of the SSCB during a fault event. At the initial moment of the fault (t_0), there is an increase in the current flowing through both the normally-on branch and the load. Upon fault detection at t_1, the cascaded JFET circuit is deactivated. This results in a rise in the voltage across the cascaded JFETs and the PCSS, while the voltage across the capacitor remains at 0 V, due to the absence of current flow through the normally-off branch. Once the voltage across the PCSS escalates beyond its threshold voltage level (V_{th}), the laser is triggered at t_2, causing the PCSS to enter a high-gain mode and conduct the fault current. The interval from t_2 to t_3 is marked by a simultaneous increase in both the capacitor voltage and the HV switch voltage, until the PCSS reaches a cut-off threshold. The PCSS ceases to conduct current, effectively concluding the turn-off transient phase.

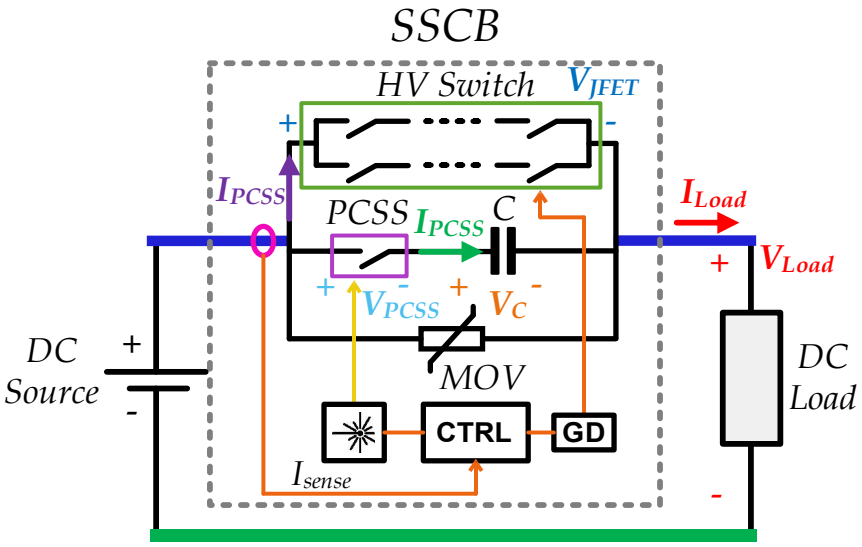

Figure 15. Conceptual breaker diagram with source and load. (Colors serve to visually differentiate the elements of the schematic).

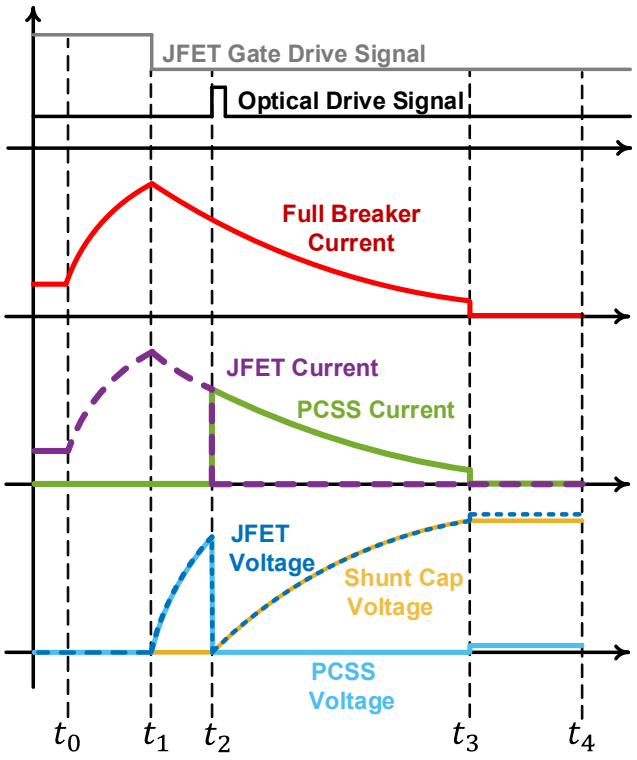

Figure 16. Idealized voltage and current timing diagram for different elements of the circuit breaker. (Colors serve to visually differentiate the elements of the schematic).

8.2. Cascaded SiC JFET Switch Topology

Figure 17a presents the circuit design of a 6 kV high-voltage (HV) switch, assembled through a series arrangement of eight 1.2 kV SiC JFET switches from UnitedSiC, UJ3N1200035K3S [94]. Seven avalanche diodes, D_1 to D_7, are strategically placed between the gates of consecutive JFETs to safeguard the transistors against overvoltage incidents. Furthermore, capacitors C_1 to C_8 are integrated between the gates of adjacent transistors, aimed at ensuring dynamic voltage balance across the drain and source terminals of the transistors. The circuit also includes two resistor branches connected between the gates of two JFETs that are sequentially separated by another JFET, with an offset of one JFET position between the two branches. These resistors are crucial for maintaining static voltage

balance across the drain and source terminals of each JFET device, enhancing the overall stability and reliability of the HV switch. Comprehensive details on the design process for each component of the proposed SSCB are documented in references [88,95].

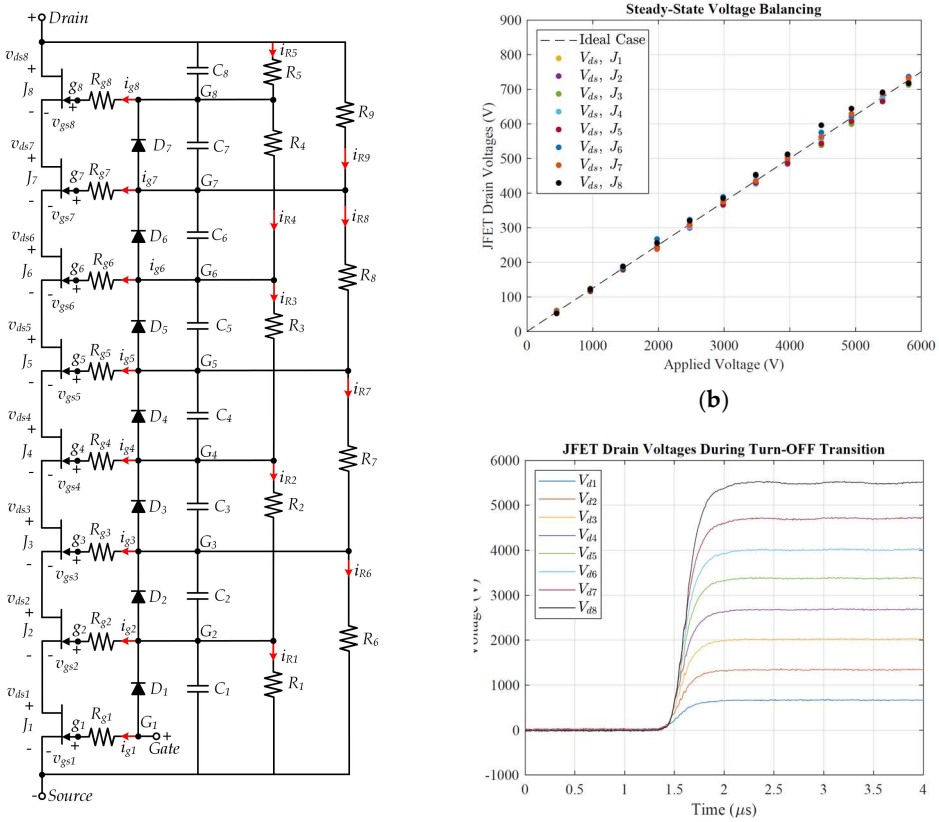

Figure 17. (**a**) HV switch is a 6 kV, normally-on device composed of a series connection of 1.2 kV SiC JFETs. (**b**) Static voltage balancing of the HV switch. (**c**) Dynamic voltage balancing of the HV switch during the turn-off transition [95].

The steady-state voltage balancing of the cascaded JFETs, across a broad spectrum of blocking voltages ranging from 500 V to 6 kV, has been assessed by measuring the drain-to-source voltage (V_{ds}) on each device. This evaluation involved comparing the experimental outcomes with the ideal scenario, which is depicted by a dashed line in Figure 17b. The comparison reveals that there is a uniform distribution of the bus voltage across the JFETs, with only slight deviations observed. Figure 17c illustrates the dynamic voltage balancing of the proposed cascaded switch during the turn-off transition at 6 kV, with a resistive load of 400 Ω connected in series. The waveforms showcased indicate uniform voltage distributions across the drain-to-source terminals of the JFETs throughout the switching transitions.

8.3. Testing of the Integrated SSCB

To verify the circuit breaker design, experiments were conducted with a 6 kV prototype, as shown in Figure 15. The setup places the breaker between a DC power supply and a resistive load, starting with the breaker in the on-state. During a turn-off transient, the breaker transitions to a high-impedance state, interrupting the DC current. The focus is on the coordinated behavior of the normally-on and normally-off sub-circuits, controlled by timing signals to the PCSS's optical driver (Nd:YAG laser) and the JFET gate driver.

The goal is to confirm the behavior depicted in Figure 16. Successful operation requires the precise timing of the PCSS activation for lock-on and current redirection from the JFET circuit. The critical parameter is the delay between the JFET trigger (t_1 in Figure 16) and

the PCSS firing (t_2 in Figure 16). The PCSS needs a minimum voltage at activation; if it fires too early, it will not lock on, and if too late, the JFET circuit bears full fault current, risking thermal stress.

The experiments differ from Figure 16 by initiating the turn-off transient from a constant current, allowing control over current magnitude by varying load impedance. Results for a successful turn-off at 6 kV are shown in Figures 18 and 19, with a line current of 5 A and the optical driver delivering 1.35 mJ of laser energy. Voltages across the breaker, shunt capacitor, and load were measured, along with currents through the circuit legs using Hall-effect probes. Figure 18 shows that the turn-off duration is dominated by the shunt capacitor's charging time.

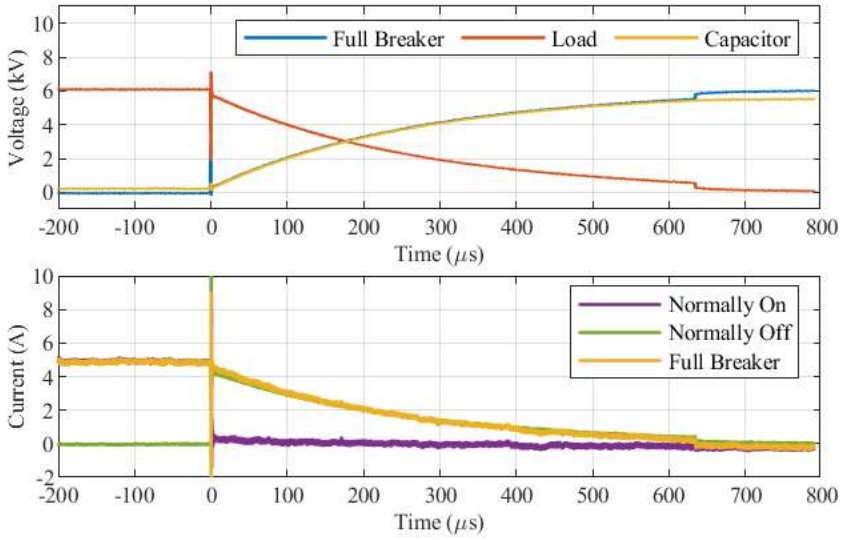

Figure 18. Longer duration turn-off transient voltage and current behavior for 6 kV hardware demonstration [96].

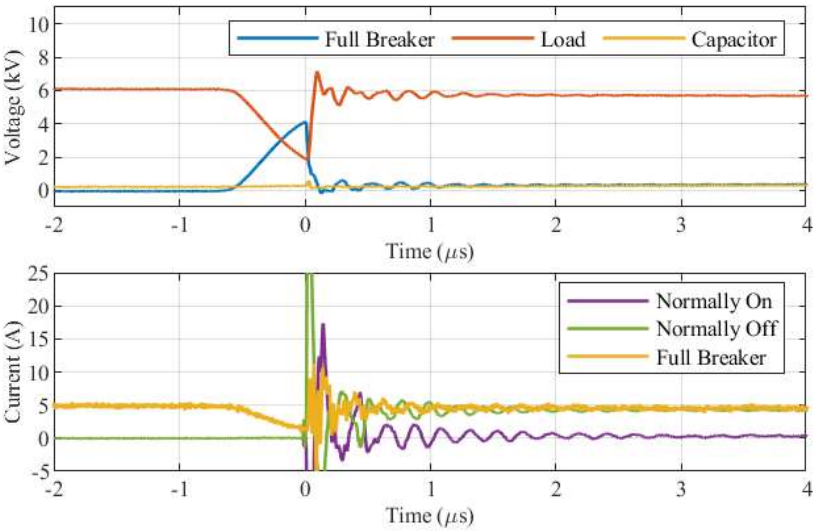

Figure 19. Shorter duration turn-off transient voltage and current behavior for the 6 kV hardware demonstration [88].

Figure 19 illustrates the coordinated behavior of the circuit legs. As the transient begins, the voltage across the JFETs rises, and once it reaches a critical threshold, the optical driver fires the PCSS. These results confirm the breaker's functionality: lock-on is achieved, diverting current into the shunt capacitor, and reducing thermal stress on the JFETs. In contrast, Figure 20 shows a 5 kV test where premature PCSS firing fails to achieve lock-on, leading to energy dissipation in the JFETs.

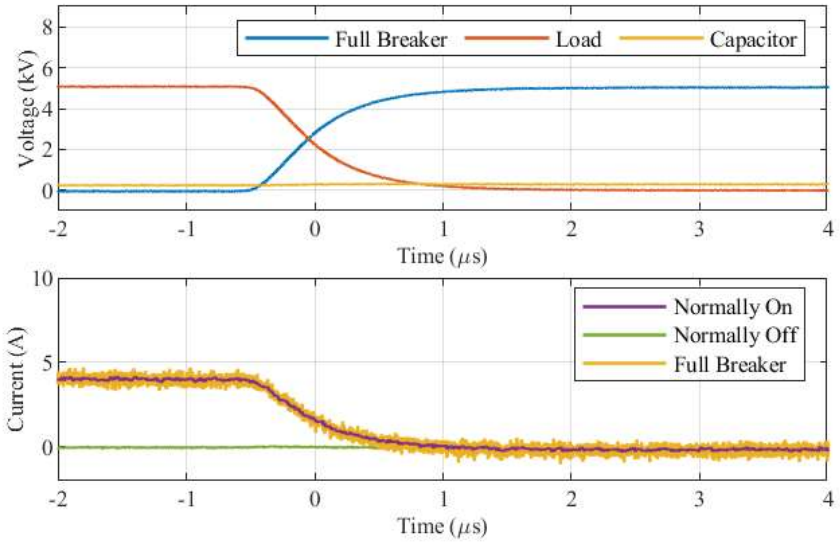

Figure 20. Shorter duration turn-off transient voltage and current behavior occurs when the PCSS optical trigger event is prematurely activated, resulting in the switch's failure to achieve lock-on behavior.

Key implications for practical implementation include the need for a precise optical driver with consistent delay for timely PCSS activation and the importance of the voltage threshold for lock-on. A larger threshold relative to the system's rated line voltage narrows the window for achieving lock-on and limits JFET stress reduction, while higher line voltages improve the chances of successful lock-on.

9. Conclusions and Outlook

While PCSS devices have been investigated since 1975, the breakthrough discovery of a nonlinear mode in GaAs only occurred in 1987. Since then, the number of materials and applications has proliferated for both direct and indirect bandgap substrates. The properties that enable tradeoffs of shot lifetime, critical field, gain, and manufacturability are presented in this work. A critical review of the physics of lock-on show it to be a potentially over-simplifying term encompassing multiple and different processes in different materials. The two qualities of unipolarity and simplicity of construction make PCSS devices an ideal vehicle for fundamental advances in the knowledge of trapping and impact ionization dynamics in the current and next-generation WBG and UWBG materials GaN, AlGaN, AlN, diamond, and β-Ga_2O_3. Despite the need for additional fundamental research into its physics, it is shown that the effect can be leveraged for highly demanding electrical utility applications. The implementation of a commercializeable circuit breaker with a normally-off GaN PCSS leg is described, opening a pathway for PCSS applications outside of the conventional domains of pulsed power.

Funding: The work described herein was funded by the ARPA-E BREAKERS program "ARC-SAFE" (grant# 18/CJ000/10/03) program directed by Isik Kizilyalli.

Data Availability Statement: Not applicable.

Acknowledgments: Sandia National Laboratories is a multi-mission laboratory managed and operated by National Technology & Engineering Solutions of Sandia, LLC (NTESS), a wholly owned subsidiary of Honeywell International Inc., for the U.S. Department of Energy's National Nuclear Security Administration (DOE/NNSA) under contract DE-NA0003525. This written work is authored by an employee of NTESS. The employee, not NTESS, owns the right, title, and interest in and to the written work and is responsible for its contents. Any subjective views or opinions that might be expressed in the written work do not necessarily represent the views of the U.S. Government. The publisher acknowledges that the U.S. Government retains a non-exclusive, paid-up, irrevocable,

Conflicts of Interest: The authors declare no conflicts of interest.

References

1. Majda-Zdancewicz, E.; Suproniuk, M.; Pawłowski, M.; Wierzbowski, M. Current state of photoconductive semiconductor switch engineering. *Opto-Electron. Rev.* **2018**, *26*, 92–102. [CrossRef]
2. Yang, Y.; Hu, L.; Yang, X.; Zhu, Z.; Huang, J.; Yang, M.; Li, X.; Ni, L.; Zhou, Y.; Geng, L. Improved Lifetime for Kilovolts Class Avalanche GaAs PCSS by Surface Passivation of Composite Dielectric Films. *IEEE Trans. Dielectr. Electr. Insul.* **2024**, 1–6. [CrossRef]
3. Zutavern, F.J.; Loubriel, G.M.; Helgeson, W.D.; O'Malley, M.W.; Gallegos, R.R.; Hjalmarson, H.P.; Baca, A.G.; Plut, T.A. *High-gain GaAs Photoconductive Semiconductor Switches (PCSS): Device Lifetime, High-Current Testing, Optical Pulse Generators*; Donaldson, W.R., Ed.; SPIE: Boston, MA, USA, 1995; pp. 146–154.
4. Mauch, D.; Sullivan, W.; Bullick, A.; Neuber, A.; Dickens, J. High Power Lateral Silicon Carbide Photoconductive Semiconductor Switches and Investigation of Degradation Mechanisms. *IEEE Trans. Plasma Sci.* **2015**, *43*, 2021–2031. [CrossRef]
5. Loubriel, G.M.; Zutavern, F.J.; Baca, A.G.; Hjalmarson, H.P.; Plut, T.A.; Helgeson, W.D.; O'Malley, M.W.; Ruebush, M.H.; Brown, D.J. Photoconductive semiconductor switches. *IEEE Trans. Plasma Sci.* **1997**, *25*, 124–130. [CrossRef]
6. Hirsch, E.A.; Mar, A.; Zutavern, F.J.; Pickrell, G.; Delhotal, J.; Gallegos, R.; Bigman, V.; Teague, J.D.; Lehr, J.M. High-Gain Persistent Nonlinear Conductivity in High-Voltage Gallium Nitride Photoconductive Switches. In Proceedings of the 2018 IEEE International Power Modulator and High Voltage Conference (IPMHVC), Jackson, WY, USA, 3–7 June 2018; IEEE: Piscataway, NJ, USA, 2018.
7. Chowdhury, A.R.; Dickens, J.C.; Neuber, A.A.; Ness, R.; Joshi, R.P. Lock-on physics in semi-insulating GaAs—Combination of trap-to-band impact ionization, moving electric fields and photon recycling. *J. Appl. Phys.* **2018**, *123*, 085703. [CrossRef]
8. Chowdhury, A.R.; Nikishin, S.; Dickens, J.; Neuber, A.; Joshi, R.P.; Ness, R. Numerical studies into the parameter space conducive to "lock-on" in a GaN photoconductive switch for high power applications. *IEEE Trans. Dielectr. Electr. Insul.* **2019**, *26*, 469–475. [CrossRef]
9. Hjalmarson, H.; Diaz, L. *Radiation Effects in Oxides and Semiconductors*; Sandia National Laboratories: Albuquerque, NM, USA, 2023.
10. Jung, H.K.; Taniguchi, K.; Hamaguchi, C. Impact ionization model for full band Monte Carlo simulation in GaAs. *J. Appl. Phys.* **1996**, *79*, 2473–2480. [CrossRef]
11. Mar, A.; Zutavern, F.; Vawter, A.; Gallegos, R.; Bigman, V.; Hjalmarson, H. *Electrical Breakdown Physics in Photoconductive Semiconductor Switches (PCSS)*; Sandia National Laboratories: Albuquerque, NM, USA, 2016.
12. Hjalmarson, H.P.; Pease, R.L.; Witczak, S.C.; Shaneyfelt, M.R.; Schwank, J.R.; Edwards, A.H.; Hembree, C.E.; Mattsson, T.R. Mechanisms for radiation dose-rate sensitivity of bipolar transistors. *IEEE Trans. Nucl. Sci.* **2003**, *50*, 1901–1909. [CrossRef]
13. Kambour, K.; Hjalmarson, H.; Zutavern, F.; Mar, A.; Myles, C.; Joshi, R. Simulation of Current Filaments in Photoconductive Semiconductor Switches. In Proceedings of the 2005 IEEE Pulsed Power Conference, Monterey, CA, USA, 13–15 June 2005; IEEE: Piscataway, NJ, USA, 2005; pp. 814–817.
14. Loubriel, G.M.; Zutavern, F.J.; Mar, A.; Hjalmarson, H.P.; Baca, A.G.; O'Malley, M.W.; Helgeson, W.D.; Falk, R.A.; Brown, D.J. Longevity of optically activated, high gain GaAs photoconductive semiconductor switches. *IEEE Trans. Plasma Sci.* **1998**, *26*, 1393–1402. [CrossRef]
15. Kambour, K.; Kang, S.; Myles, C.W.; Hjalmarson, H.P. Steady state properties of lock-on current filaments in GaAs [pulsed power switches]. In Proceedings of the Digest of Technical Papers. 12th IEEE International Pulsed Power Conference (Cat. No.99CH36358), Monterey, CA, USA, 27–30 June 1999; IEEE: Piscataway, NJ, USA, 1999; Volume 2, pp. 791–794.
16. Brinkmann, R.P.; Schoenbach, K.H.; Stoudt, D.C.; Lakdawala, V.K.; Gerdin, G.A.; Kennedy, M.K. The lock-on effect in electron-beam-controlled gallium arsenide switches. *IEEE Trans. Electron Devices* **1991**, *38*, 701–705. [CrossRef]
17. Hjalmarson, H.P.; Zutavern, F.J.; Williamson, K.M.; Lehr, J.M.; Pineda, A.C. Electrical breakdown phenomena involving material interfaces. In Proceedings of the 2013 19th IEEE Pulsed Power Conference (PPC), San Francisco, CA, USA, 16–21 June 2013; IEEE: Piscataway, NJ, USA, 2013; pp. 1–5.
18. Stoklas, R.; Chvala, A.; Sichman, P.; Hasenohrl, S.; Hascik, S.; Priesol, J.; Satka, A.; Kuzmik, J. Analysis and Modeling of Vertical Current Conduction and Breakdown Mechanisms in Semi-Insulating GaN Grown on GaN: Role of Deep Levels. *IEEE Trans. Electron Devices* **2021**, *68*, 2365–2371. [CrossRef]
19. Stout, P.J.; Kushner, M.J. Characteristics of an optically activated pulsed power GaAs(Si:Cu) switch obtained by two-dimensional modeling. *J. Appl. Phys.* **1995**, *77*, 3518–3522. [CrossRef]

20. Schultz, P.A.; Edwards, A.H.; Van Ginhoven, R.M.; Hjalmarson, H.P.; Mounce, A.M. Theory of magnetic 3 d transition metal dopants in gallium nitride. *Phys. Rev. B* **2023**, *107*, 205202. [CrossRef]
21. Maeda, T.; Narita, T.; Yamada, S.; Kachi, T.; Kimoto, T.; Horita, M.; Suda, J. Impact ionization coefficients and critical electric field in GaN. *J. Appl. Phys.* **2021**, *129*, 185702. [CrossRef]
22. Doğan, S.; Teke, A.; Huang, D.; Morkoç, H.; Roberts, C.B.; Parish, J.; Ganguly, B.; Smith, M.; Myers, R.E.; Saddow, S.E. 4H–SiC photoconductive switching devices for use in high-power applications. *Appl. Phys. Lett.* **2003**, *82*, 3107–3109. [CrossRef]
23. Kelkar, K.S.; Islam, N.E.; Fessler, C.M.; Nunnally, W.C. Silicon carbide photoconductive switch for high-power, linear-mode operations through sub-band-gap triggering. *J. Appl. Phys.* **2005**, *98*, 093102. [CrossRef]
24. Sullivan, J.S.; Stanley, J.R. Wide Bandgap Extrinsic Photoconductive Switches. *IEEE Trans. Plasma Sci.* **2008**, *36*, 2528–2532. [CrossRef]
25. Quast, J.; Hansen, D.; Loboda, M.; Manning, I.; Moeggenborg, K.; Mueller, S.; Parfeniuk, C.; Sanchez, E.; Whiteley, C. High Quality 150 mm 4H SiC Wafers for Power Device Production. *Mater. Sci. Forum* **2015**, *821–823*, 56–59. [CrossRef]
26. Evwaraye, A.O.; Smith, S.R.; Mitchel, W.C. Determination of the band offsets of the 4H–SiC/6H–SiC heterojunction using the vanadium donor (0/+) level as a reference. *Appl. Phys. Lett.* **1995**, *67*, 3319–3321. [CrossRef]
27. Baur, J.; Kunzer, M.; Schneider, J. Transition Metals in SiC Polytypes, as Studied by Magnetic Resonance Techniques. *Phys. Status Solidi A* **1997**, *162*, 153–172. [CrossRef]
28. Mitchel, W.C.; Perrin, R.; Goldstein, J.; Saxler, A.; Roth, M.; Smith, S.R.; Solomon, J.S.; Evwaraye, A.O. Fermi level control and deep levels in semi-insulating 4H–SiC. *J. Appl. Phys.* **1999**, *86*, 5040–5044. [CrossRef]
29. Dalibor, T.; Pensl, G.; Matsunami, H.; Kimoto, T.; Choyke, W.J.; Schöner, A.; Nordell, N. Deep Defect Centers in Silicon Carbide Monitored with Deep Level Transient Spectroscopy. *Phys. Status Solidi A* **1997**, *162*, 199–225. [CrossRef]
30. Mitchel, W.C.; Mitchell, W.D.; Landis, G.; Smith, H.E.; Lee, W.; Zvanut, M.E. Vanadium donor and acceptor levels in semi-insulating 4H- and 6H-SiC. *J. Appl. Phys.* **2007**, *101*, 013707. [CrossRef]
31. Rakheja, S.; Huang, L.; Hau-Riege, S.; Harrison, S.E.; Voss, L.F.; Conway, A.M. Performance Modeling of Silicon Carbide Photoconductive Switches for High-Power and High-Frequency Applications. *IEEE J. Electron Devices Soc.* **2020**, *8*, 1118–1128. [CrossRef]
32. Kramer, N.J.; Voss, L.F.; Conway, A.M.; Grivickas, P.V.; Bora, M.; Hall, D.L.; Caruso, A.N. Extrinsic Absorption Pathways in Vanadium-Doped SiC Measured Using a Total Internal Reflection Geometry. *Phys. Status Solidi A* **2020**, *217*, 2000315. [CrossRef]
33. Hemmat, Z.; Faez, R.; Moreno, E.; Rasouli, F.; Radfar, F.; Zaimbashi, M. Transient and steady state study of a rear-illuminated 6H-SiC Photoconductive Semiconductor Switch. *Optik* **2016**, *127*, 4615–4620. [CrossRef]
34. Mauch, D.; White, C.; Thomas, D.; Neuber, A.; Dickens, J. Overview of high voltage 4H-SiC photoconductive semiconductor switch efforts at Texas Tech University. In Proceedings of the 2014 IEEE International Power Modulator and High Voltage Conference (IPMHVC), Santa Fe, NM, USA, 1–5 June 2014; 2014; pp. 23–26.
35. Gradinaru, G.; Sudarshan, T.S. A review on the breakdown limitation of photoconductive semiconductor power switches. In Proceedings of the 9th IEEE International Pulsed Power Conference, Albuquerque, NM, USA, 21–23 June 1993; Volume 2, p. 645.
36. Sullivan, J.S. High power operation of a nitrogen doped, vanadium compensated, 6H-SiC extrinsic photoconductive switch. *Appl. Phys. Lett.* **2014**, *104*, 172106. [CrossRef]
37. Cao, P.; Huang, W.; Guo, H.; Zhang, Y. Performance of a Vertical 4H-SiC Photoconductive Switch with AZO Transparent Conductive Window and Silver Mirror Reflector. *IEEE Trans. Electron Devices* **2018**, *65*, 2047–2051. [CrossRef]
38. Bora, M.; Voss, L.F.; Grivickas, P.V.; Hall, D.L.; Alameda, J.B.; Kramer, N.J.; Torres, A.M.; Conway, A.M. A Total Internal Reflection Photoconductive Switch. *IEEE Electron Device Lett.* **2019**, *40*, 734–737. [CrossRef]
39. Wang, B.; Wang, L.; Niu, X.; Chu, X.; Yi, M.; Yao, J.; Xun, T. Breakdown behavior of SiC photoconductive switch with transparent electrode. *AIP Adv.* **2022**, *12*, 085210. [CrossRef]
40. Wang, L.; Chu, X.; Wu, Q.; Xun, T.; Yang, H.; He, J.; Zhang, J. Effects of High-Field Velocity Saturation on the Performance of V-Doped 6H Silicon-Carbide Photoconductive Switches. *IEEE J. Emerg. Sel. Top. Power Electron.* **2021**, *9*, 4879–4886. [CrossRef]
41. Wu, Q.; Xun, T.; Zhao, Y.; Yang, H.; Huang, W. The Test of a High-Power, Semi-Insulating, Linear-Mode, Vertical 6H-SiC PCSS. *IEEE Trans. Electron Devices* **2019**, *66*, 1837–1842. [CrossRef]
42. Han, Z.; Lee, J.; Messing, S.; Reboli, T.; Mironov, A.; Bayram, C. High Current Density Diamond Photoconductive Semiconductor Switches with a Buried, Metallic Conductive Channel. *IEEE Electron Device Lett.* **2024**, *45*, 1044–1047. [CrossRef]
43. Bharadwaj, P.K.; Code, R.F.; van Driel, H.M.; Walentynowicz, E. High voltage optoelectronic switching in diamond. *Appl. Phys. Lett.* **1983**, *43*, 207–209. [CrossRef]
44. Donato, N.; Rouger, N.; Pernot, J.; Longobardi, G.; Udrea, F. Diamond power devices: State of the art, modelling, figures of merit and future perspective. *J. Phys. Appl. Phys.* **2019**, *53*, 093001. [CrossRef]
45. Woo, K.; Malakoutian, M.; Reeves, B.A.; Chowdhury, S. A study on sub-bandgap photoexcitation in nitrogen- and boron-doped diamond with interdigitated device structure. *Appl. Phys. Lett.* **2022**, *120*, 112104. [CrossRef]

46. Curry, J.J.; Feng, S.T.; Lee, C.H.; Ho, P.T.; Goldhar, J. *Photoconductive Switching in Diamond Under High Bias*; Pinnow, D., Moulton, P., Eds.; Optica Publishing Group: Anaheim, CA, USA, 1988; Volume 7, p. TUM50.
47. Isberg, J.; Hammersberg, J.; Johansson, E.; Wikström, T.; Twitchen, D.J.; Whitehead, A.J.; Coe, S.E.; Scarsbrook, G.A. High Carrier Mobility in Single-Crystal Plasma-Deposited Diamond. *Science* **2002**, *297*, 1670–1672. [CrossRef]
48. Prasad, R.R.; Schein, J.; Gensler, S.W.; Krishnan, M. Optically Triggered Diamond Switches. In Proceedings of the Digest of Technical Papers. 12th IEEE International Pulsed Power Conference (Cat. No.99CH36358), Monterey, CA, USA, 27–30 June 1999; IEEE: Piscataway, NJ, USA, 1999; Volume 1, pp. 142–145.
49. Yoneda, H.; Tokuyama, K.; Ueda, K.; Yamamoto, H.; Baba, K. High-power terahertz radiation emitter with a diamond photoconductive switch array. *Appl. Opt.* **2001**, *40*, 6733–6736. [CrossRef] [PubMed]
50. Collins, A.T.; Connor, A.; Ly, C.-H.; Shareef, A.; Spear, P.M. High-temperature annealing of optical centers in type-I diamond. *J. Appl. Phys.* **2005**, *97*, 083517. [CrossRef]
51. Grivickas, P.; Ščajev, P.; Kazuchits, N.; Mazanik, A.; Korolik, O.; Voss, L.F.; Conway, A.M.; Hall, D.L.; Bora, M.; Subačius, L.; et al. Carrier recombination parameters in diamond after surface boron implantation and annealing. *J. Appl. Phys.* **2020**, *127*, 245707. [CrossRef]
52. Hall, D.L.; Voss, L.F.; Grivickas, P.; Bora, M.; Conway, A.M.; Ščajev, P.; Grivickas, V. Photoconductive Switch with High Sub-Bandgap Responsivity in Nitrogen-Doped Diamond. *IEEE Electron Device Lett.* **2020**, *41*, 1070–1073. [CrossRef]
53. Murooka, T.; Shiigai, M.; Hironaka, Y.; Tsuji, T.; Yang, B.; Hoang, T.M.; Suda, K.; Mizuno, K.; Kato, H.; Makino, T.; et al. Photoelectrical detection of nitrogen-vacancy centers by utilizing diamond lateral p–i–n diodes. *Appl. Phys. Lett.* **2021**, *118*, 253502. [CrossRef]
54. Bourgeois, E.; Jarmola, A.; Siyushev, P.; Gulka, M.; Hruby, J.; Jelezko, F.; Budker, D.; Nesladek, M. Photoelectric detection of electron spin resonance of nitrogen-vacancy centres in diamond. *Nat. Commun.* **2015**, *6*, 8577. [CrossRef]
55. Heinselman, K.N.; Haven, D.; Zakutayev, A.; Reese, S.B. Projected Cost of Gallium Oxide Wafers from Edge-Defined Film-Fed Crystal Growth. *Cryst. Growth Des.* **2022**, *22*, 4854–4863. [CrossRef]
56. Higashiwaki, M.; Kuramata, A.; Murakami, H.; Kumagai, Y. State-of-the-art technologies of gallium oxide power devices. *J. Phys. Appl. Phys.* **2017**, *50*, 333002. [CrossRef]
57. Sasaki, K.; Kuramata, A.; Masui, T.; Víllora, E.G.; Shimamura, K.; Yamakoshi, S. Device-Quality β-Ga_2O_3 Epitaxial Films Fabricated by Ozone Molecular Beam Epitaxy. *Appl. Phys. Express* **2012**, *5*, 035502. [CrossRef]
58. Mcglone, J.F.; Xia, Z.; Zhang, Y.; Joishi, C.; Lodha, S.; Rajan, S.; Ringel, S.A.; Arehart, A.R. Trapping Effects in Si δ-Doped β-Ga_2O_3 MESFETs on an Fe-Doped β-Ga_2O_3 Substrate. *IEEE Electron Device Lett.* **2018**, *39*, 1042–1045. [CrossRef]
59. Polyakov, A.Y.; Nikolaev, V.I.; Yakimov, E.B.; Ren, F.; Pearton, S.J.; Kim, J. Deep level defect states in β-, α-, and ε -Ga_2O_3 crystals and films: Impact on device performance. *J. Vac. Sci. Technol. A* **2022**, *40*, 020804. [CrossRef]
60. Bhandari, S.; Zvanut, M.E. Charge trapping at Fe due to midgap levels in Ga_2O_3. *J. Appl. Phys.* **2021**, *129*, 085703. [CrossRef]
61. Dowling, K.M.; Chatterjee, B.; Ghandiparsi, S.; Shao, Q.; Varley, J.; Schneider, J.D.; Chapin, C.; Gottlieb, M.S.; Leos, L.; Sword, M.; et al. Evaluation of Fe-βGa_2O_3 for Photoconductive Semiconductor Switching. *IEEE Trans. Electron Devices* **2024**, *71*, 1535–1540. [CrossRef]
62. Bhandari, S.; Zvanut, M.E.; Varley, J.B. Optical absorption of Fe in doped Ga_2O_3. *J. Appl. Phys.* **2019**, *126*, 165703. [CrossRef]
63. Wang, Z.; Chen, X.; Ren, F.-F.; Gu, S.; Ye, J. Deep-level defects in gallium oxide. *J. Phys. Appl. Phys.* **2020**, *54*, 043002. [CrossRef]
64. Zimmermann, C.; Kalmann Frodason, Y.; Rønning, V.; Varley, J.B.; Vines, L. Combining steady-state photo-capacitance spectra with first-principles calculations: The case of Fe and Ti in β-Ga_2O_3. *New J. Phys.* **2020**, *22*, 063033. [CrossRef]
65. Singh, A.; Koksal, O.; Tanen, N.; McCandless, J.; Jena, D.; Xing, H.; Peelaers, H.; Rana, F. Ultrafast dynamics of gallium vacancy charge states in beta Ga_2O_3. *Phys. Rev. Res.* **2021**, *3*, 023154. [CrossRef]
66. Nunnally, W.C.; Hammond, R.B. Photoconductive Power Switches. In Proceedings of the 27th Annual Technical Symposium, San Diego, CA, USA, 23–25 August 1983; Mourou, G.A., Ed.; SPIE: Bellingham, WA, USA; pp. 116–122.
67. Kawase, T.; Hagi, Y.; Tatsumi, M.; Fujita, K.; Nakai, R. Low-dislocation-density and low-residual-strain semi-insulating GaAs grown by vertical boat method. In Proceedings of the Semiconducting and Semi-Insulating Materials Conference, Toulouse, France, 29 April–3 May 1996; IEEE: Piscataway, NJ, USA, 1996; pp. 275–278.
68. Bünger, T.; Behr, D.; Eichler, S.; Flade, T.; Fliegel, W.; Jurisch, M.; Kleinwechter, A.; Kretzer, U.; Steinegger, T.; Weinert, B. Development of a vertical gradient freeze process for low EPD GaAs substrates. *Mater. Sci. Eng. B* **2001**, *80*, 5–9. [CrossRef]
69. Wang, X.; Mazumder, S.K. A photoconductive semiconductor switch vertically embedded with MISFETs for high-power high-repetition-rate application. In Proceedings of the 2015 IEEE 6th International Symposium on Power Electronics for Distributed Generation Systems (PEDG), Aachen, Germany, 22–25 June 2015; IEEE: Piscataway, NJ, USA, 2015; pp. 1–5.
70. Gaudet, J.A.; Prather, W.D.; Burger, J.; Skipper, M.C.; Abdalla, M.D.; Mar, A.; O'Malley, M.W.; Zutavern, F.J.; Loubriel, G.M. Progress in gallium arsenide photoconductive switch research for high power applications. In Proceedings of the Conference Record of the Twenty-Fifth International Power Modulator Symposium, 2002 and 2002 High-Voltage Workshop, Hollywood, CA, USA, 30 June–3 July 2002; IEEE: Piscataway, NJ, USA, 2002; pp. 699–702.

71. Shi, W.; Tian, L.; Liu, Z.; Zhang, L.; Zhang, Z.; Zhou, L.; Liu, H.; Xie, W. 30 kV and 3 kA semi-insulating GaAs photoconductive semiconductor switch. *Appl. Phys. Lett.* **2008**, *92*, 043511. [CrossRef]
72. Zutavern, F.J.; Glover, S.F.; Mar, A.; Cich, M.J.; Loubriel, G.M.; Swalby, M.E.; Collins, R.T.; Greives, K.H.; Keator, N.D. High current, multi-filament photoconductive semiconductor switching. In Proceedings of the 2011 IEEE Pulsed Power Conference, Chicago, IL, USA, 19–23 June 2011; IEEE: Piscataway, NJ, USA, 2011; pp. 1112–1119.
73. Mar, A.; Zutavern, F.; Hjalmarson, H.; Vawter, G.A.; Gallegos, R. *Advanced High-Longevity GaAs Photoconductive Semiconductor Switches*; Directed Energy Professional Society: Anaheim, CA, USA, 2015.
74. Loubriel, G.M.; Omalley, M.M.; Zutavern, F.J. Toward pulsed power uses for photoconductive semiconductor switches: Closing switches. In Proceedings of the 6th Institute of Electrical and Electronic Engineers Pulsed Power Conference, Arlington, VA, USA, 29 June–1 July 1987; IEEE: Piscataway, NJ, USA, 1987.
75. Zutavern, F.J.; Loubriel, G.M.; McLaughlin, D.L.; Helgeson, W.D.; O'Malley, M.W. Electrical and optical properties of high-gain GaAs switches. In Proceedings of the OE/LASE '92, Los Angeles, CA, USA, 19–24 January 1992; Loubriel, G.M., Ed.; SPIE: Bellingham, WA, USA, 1992; p. 152.
76. Schoenberg, J.S.H.; Burger, J.W.; Tyo, J.S.; Abdalla, M.D.; Skipper, M.C.; Buchwald, W.R. Ultra-wideband source using gallium arsenide photoconductive semiconductor switches. *IEEE Trans. Plasma Sci.* **1997**, *25*, 327–334. [CrossRef]
77. Lehr, J.M.; Ahern, S.M.; Abdalla, M.D.; Skipper, M.C.; Romero, S.P.; Gaudet, J.A.; Burger, J.W.; Hull, J.P.; Gruner, F.R.; Cockerham, B.D.; et al. Marx generator triggering with photoconductive switches. In Proceedings of the AeroSense 2000, Orlando, FL, USA, 24–28 April 2000; Brandt, H.E., Ed.; SPIE: Bellingham, WA, USA, 2000; pp. 175–184.
78. Amano, H.; Baines, Y.; Beam, E.; Borga, M.; Bouchet, T.; Chalker, P.R.; Charles, M.; Chen, K.J.; Chowdhury, N.; Chu, R.; et al. The 2018 GaN power electronics roadmap. *J. Phys. Appl. Phys.* **2018**, *51*, 163001. [CrossRef]
79. Koehler, A.D.; Anderson, T.J.; Khachatrian, A.; Nath, A.; Tadjer, M.J.; Buchner, S.P.; Hobart, K.D.; Kub, F.J. High Voltage GaN Lateral Photoconductive Semiconductor Switches. *ECS J. Solid State Sci. Technol.* **2017**, *6*, S3099. [CrossRef]
80. Chen, Y.; Lu, H.; Chen, D.; Ren, F.; Zhang, R.; Zheng, Y. High-voltage photoconductive semiconductor switches fabricated on semi-insulating HVPE GaN:Fe template. *Phys. Status Solidi C* **2016**, *13*, 374–377. [CrossRef]
81. Meyers, V.; Mauch, D.; Kuryatkov, V.; Nikishin, S.; Dickens, J.; Neuber, A.; Ness, R. Toward the development of an efficient bulk semi-insulating GaN photoconductive switch. In Proceedings of the 2017 IEEE 21st International Conference on Pulsed Power (PPC), Brighton, UK, 18–22 June 2017; IEEE: Piscataway, NJ, USA, 2017; pp. 1–4.
82. Liu, G.; Zhou, G.; Qin, Z.; Zhou, Q.; Zheng, R.; Wu, H.; Sun, Z. Luminescence characterizations of freestanding bulk single crystalline aluminum nitride towards optoelectronic application. *CrystEngComm* **2017**, *19*, 5522–5527. [CrossRef]
83. Bondokov, R.T.; Hogan, K.; Norbury, G.Q.; Mark, J.; Branagan, S.P.; Ishigami, N.; Grandusky, J.; Chen, J. (Jeff) (Invited) Development of 3-inch AlN Single Crystal Substrates. *ECS Trans.* **2022**, *109*, 13–19. [CrossRef]
84. Meyer, J.R.; Kruer, M.R.; Bartoli, F.J. Optical heating in semiconductors: Laser damage in Ge, Si, InSb, and GaAs. *J. Appl. Phys.* **1980**, *51*, 5513–5522. [CrossRef]
85. Nune, R.; Anurag, A.; Anand, S.; Chauhan, Y.S. Comparative analysis of power density in Si MOSFET and GaN HEMT based flyback converters. In Proceedings of the 2016 10th International Conference on Compatibility, Power Electronics and Power Engineering (CPE-POWERENG), Bydgoszcz, Poland, 29 June–1 July 2016; IEEE: Piscataway, NJ, USA, 2016; pp. 347–352.
86. BREAKERS: Building Reliable Electronics to Achieve Kilovolt Effective Ratings Safely. Available online: https://arpa-e.energy.gov/technologies/programs/breakers (accessed on 9 December 2023).
87. Lehr, J.; Gonzalez, N.; Maynard, B.; Gallegos, R.; Hjalmarson, H.; Kaplar, R.; Mar, A.; Schrock, E.; Pickrell, G. *Investigating Lock on in Gallium Nitride Photoconductive Solid State Switches*; Sandia National Lab. (SNL-NM): Albuquerque, NM, USA, 2021; No. SAND2021-15818C.
88. Flicker, J.D.; Garcia Rodriguez, L.A.; Mueller, J.; Gill, L.; Neely, J.C.; Schrock, E.; Hjalmarson, H.P.; Bellotti, E.; Schultz, P.A.; Lehr, J.M.; et al. Light-Triggered Solid-State Circuit Breaker for DC Electrical Systems. In *Direct Current Fault Protection*; Kizilyalli, I.C., Shen, Z.J., Cunningham, D.W., Eds.; Springer International Publishing: Cham, Switzerland, 2023; pp. 185–222. ISBN 978-3-031-26571-6.
89. Korotkov, R.Y.; Gregie, J.M.; Wessels, B.W. Optical properties of the deep Mn acceptor in GaN:Mn. *Appl. Phys. Lett.* **2002**, *80*, 1731–1733. [CrossRef]
90. Yao, X. Study on DC arc faults in ring-bus DC microgrids with constant power loads. In Proceedings of the 2016 IEEE Energy Conversion Congress and Exposition (ECCE), Milwaukee, WI, USA, 18–22 September 2016; IEEE: Piscataway, NJ, USA, 2016; pp. 1–5.
91. Baran, M.E.; Mahajan, N.R. DC distribution for industrial systems: Opportunities and challenges. *IEEE Trans. Ind. Appl.* **2003**, *39*, 1596–1601. [CrossRef]
92. Pei, X.; Cwikowski, O.; Vilchis-Rodriguez, D.S.; Barnes, M.; Smith, A.C.; Shuttleworth, R. A review of technologies for MVDC circuit breakers. In Proceedings of the IECON 2016—42nd Annual Conference of the IEEE Industrial Electronics Society, Florence, Italy, 23–26 October 2016; IEEE: Piscataway, NJ, USA, 2016; pp. 3799–3805.

93. Shukla, A.; Demetriades, G.D. A Survey on Hybrid Circuit-Breaker Topologies. *IEEE Trans. Power Deliv.* **2015**, *30*, 627–641. [CrossRef]
94. *35 mΩ-1200V SiC Normally-On JFET, UJ3N120035K3S*; Qorvo (formerly United SiC): Greensboro, NC, USA, 2018.
95. Garcia Rodriguez, L.A.; Gill, L.; Mueller, J.A.; Neely, J.; Baker, G.; Flicker, J.; Schrock, E.; Pickrell, G.; Kaplar, R. Cascaded SiC JFET Topology for High-Voltage Solid-State Circuit Breaker Applications. *IEEE Trans. Ind. Appl.* **2023**, *59*, 2326–2339. [CrossRef]
96. Zutavern, F.J.; Glover, S.F.; Reed, K.W.; Cich, M.J.; Mar, A.; Swalby, M.E.; Saiz, T.A.; Horry, M.L.; Gruner, F.R.; White, F.E. PCSS triggered pulsed power switches. In Proceedings of the 2007 16th IEEE International Pulsed Power Conference, Albuquerque, NM, USA, 17–22 June 2007; IEEE: Piscataway, NJ, USA, 2007; pp. 231–235.